JOURNAL OF PETROLOGY

Journal of Petrology, 2015, Vol. 56, No. 9, 1677–1702
doi: 10.1093/petrology/egv050
Advance Access Publication Date: 6 October 2015
Original Article

OXFORD

Timing of Partial Melting and Cooling across the Greater Himalayan Crystalline Complex (Nyalam, Central Himalaya): In-sequence Thrusting and its Implications

Jia-Min Wang[1,2], Daniela Rubatto[2] and Jin-Jiang Zhang[1,*]

[1]Key Laboratory of Orogenic Belts and Crustal Evolution, School of Earth and Space Sciences, Peking University, Beijing 100871, China and [2]Research School of Earth Sciences, Australian National University, Canberra, ACT 2601, Australia

*Corresponding author. Telephone: +86 10 62754368. E-mail: zhjj@pku.edu.cn

Received November 26, 2014; Accepted August 4, 2015

ABSTRACT

The timing of crustal melting and cooling has been investigated across the migmatites of the Greater Himalayan Crystalline Complex (GHC) in the Nyalam region, central Himalaya. Monazite U–Pb ages vary from 32 to 14 Ma and are linked to metamorphic conditions on the basis of monazite internal zoning, mineral inclusions, and changes in heavy rare earth element and Y composition. Metamorphic temperatures were estimated by Zr-in-rutile thermometry and cooling rates were further constrained by rutile U–Pb ages. The results reveal two distinct blocks within the GHC of the Nyalam region. The upper GHC experienced higher peak metamorphic temperatures (730–750°C) and a higher degree of melting (15–25%). Partial melting was dominated by muscovite dehydration melting, which lasted from ~32 to 25 Ma, possibly until ~20 Ma. The lower GHC experienced lower peak metamorphic temperatures (640–675°C) and a lower degree of melting (0–10%) mainly via H_2O-saturated melting from 19 to 16 Ma. At different times, both upper and lower blocks experienced initial slow cooling (rates 35 ± 8 and 10 ± 5°C Ma^{-1}, respectively) followed by rapid cooling (100 ± 20°C Ma^{-1}). The documented diachronous metamorphism implies the presence of the 'High Himalayan Thrust' that was active at ~25–16 Ma within the GHC of the central Himalaya. Different degrees and durations of partial melting in the investigated section suggest that a channel flow process dominated the exhumation of the upper GHC migmatites at 25–16 Ma, whereas a critical taper process dominated the exhumation of the relatively lower-grade lower GHC rocks and cooled upper GHC migmatites at 16–10 Ma. We suggest that propagating thrusts along large tectonic boundaries together with low-viscosity lateral crustal flow could contribute to exhumation of high-grade metamorphic rocks in the Himalaya and other similar collisional orogens.

Key words: monazite; partial melting; trace elements; tectonic discontinuity; U–Pb geochronology

INTRODUCTION

Burial and exhumation of high-grade metamorphic rocks in collisional settings has major implications for the thermal evolution of orogens and the crust in general (e.g. England & Thompson, 1984; Beaumont *et al.*, 2001; Faccenda *et al.*, 2008; Kohn, 2008). Despite numerous case studies and numerical simulations, our knowledge of the factors that regulate the exhumation of high-grade metamorphic rocks is still limited. Traditional models focused on propagating thrusts, which form along failures in shortening orogens and are considered to be responsible for exhuming hanging-wall rocks and burying footwall rocks (England & Thompson, 1984; Royden, 1993; Henry *et al.*, 1997). Recent thermal–mechanical models highlight the contribution of partial melting, suggesting that it has the

capacity to lower the viscosity and density of crustal rocks and can thus trigger exhumation (Beaumont *et al.*, 2001; Jamieson *et al.*, 2004; Faccenda *et al.*, 2008).

As the youngest and one of the largest continent–continent collisional orogens on the planet, the Himalaya are the best natural laboratory to investigate burial and exhumation processes. The Himalaya are being formed by the continuing collision of India and Asia since 50–55 Ma (Rowley, 1996; Leech *et al.*, 2005) and have not been overprinted by a later orogenic event. The orogen is relatively young so that modern geochronology can accurately distinguish different stages of evolution, which may not be resolvable for older orogens. The issue discussed above lies between two end-member models: (1) the critical taper model (DeCelles *et al.*, 2001; Kohn *et al.*, 2004; Bollinger *et al.*, 2006; Robinson *et al.*, 2006; Kohn, 2008; Corrie & Kohn, 2011) assumes the orogen to be a Coulomb wedge and supports propagating thrusting to dominate exhumation of the Greater Himalayan Crystalline Complex (GHC); (2) the channel flow model (Nelson *et al.*, 1996; Beaumont *et al.*, 2001; Searle *et al.*, 2003; Jamieson *et al.*, 2004; Searle & Szulc, 2005; Godin *et al.*, 2006) proposes that low-viscosity crustal melts and focused surface erosion triggered exhumation of the GHC, with coeval movement along bounding structures of the Main Central Thrust (MCT) and South Tibetan Detachment (STD); (3) a third scenario suggests that the channel flow and critical taper processes are not mutually exclusive, but that the dominant process changes through time as the orogen evolves (Beaumont & Jamieson, 2010; Larson *et al.*, 2010, 2011; Jamieson & Beaumont, 2013).

Although a large number of studies have been made of the GHC, the debate between the proponents of the two main tectonic models continues (e.g. Kohn, 2008; Chambers *et al.*, 2011; Montomoli *et al.*, 2013). To better evaluate the models, the following crucial questions need to be answered.

1. Is metamorphism across the GHC diachronous or synchronous and what is the duration of melting and high-temperature metamorphism? Specifically, the critical taper model supports diachronous metamorphism and a short residence time (~5 Myr) at high temperatures across the GHC (Kohn, 2008), whereas the original channel flow model predicts synchronous metamorphism and high temperatures lasting for 10–15 Myr (Beaumont *et al.*, 2001; Jamieson *et al.*, 2004).
2. If channel flow and critical taper processes coexist during the exhumation of the GHC, then how does the dominant process evolve spatially and temporally? Some studies have proposed a transition from channel flow to a critical taper process during the exhumation of the GHC (e.g. Larson *et al.*, 2010, 2011), but better spatial–temporal resolution of each process is still required.

Among the various approaches used to answer the above questions, age determination using accessory minerals provides crucial information. Successful studies in the Himalaya and other high-temperature terranes have used U–Th–Pb dating of accessory minerals that (re)crystallized at different points along *P–T* trajectories to reconstruct the metamorphic process or timescale of partial melting (e.g. Foster *et al.*, 2000; Rubatto *et al.*, 2001, 2013; Larson *et al.*, 2011; Imayama *et al.*, 2012; From *et al.*, 2014; Larson & Cottle, 2014). Geochronology also plays an important role in identifying hidden discontinuities that may be difficult to identify using structures or metamorphic grade (Harrison *et al.*, 1997; Kohn *et al.*, 2004; Imayama *et al.*, 2012; Rubatto *et al.*, 2013). Among the various datable accessory minerals, monazite is a preferred chronometer for Himalayan metamorphic rocks because of (1) its abundance in Himalayan metapelites, (2) its reactivity, particularly compared with zircon, during amphibolite-facies metamorphism, (3) its complex growth mechanism, which has the potential to record various stages along the *P–T* trajectory (Foster *et al.*, 2000; Hermann & Rubatto, 2003; Williams *et al.*, 2007), and (4) its robustness to high-temperature resetting by diffusion (~900°C, Cherniak *et al.*, 2004).

Despite the fact that monazite U–Th–Pb geochronology has been used for decades (e.g. Schärer, 1984; Parrish, 1990; Harrison *et al.*, 1995), age interpretation still represents a challenge, especially for metamorphic rocks. Previous attempts to link monazite ages to metamorphic conditions have used different tools, as follows.

1. *In situ* dating can provide clear temporal relationships between monazite and garnet porphyroblasts or matrix minerals (Harrison *et al.*, 1997; Foster *et al.*, 2000; Catlos *et al.*, 2002; Kohn & Malloy, 2004).
2. Y and heavy rare earth element (HREE) signatures can relate monazite formation to garnet growth or breakdown. This includes monazite Y compositional mapping by electron microprobe (EMP) (Foster *et al.*, 2002; Kohn *et al.*, 2004; Kellett *et al.*, 2010; Corrie & Kohn, 2011; Stearns *et al.*, 2013) or monitoring HREE signatures of dated growth zones (Hermann & Rubatto, 2003; Buick *et al.*, 2006; Rubatto *et al.*, 2006, 2013).
3. A third approach investigates monazite-forming reactions and conditions (Wing *et al.*, 2003; Kohn & Malloy, 2004; Janots *et al.*, 2007; Spear & Pyle, 2010).
4. In selected cases, the monazite–xenotime–garnet Y equilibrium thermometer can directly provide metamorphic temperatures for monazite growth (Pyle *et al.*, 2001; Foster *et al.*, 2004).

Interpretations that are not well constrained by some of the above criteria could easily mix prograde, peak or retrograde ages and thus prevent the resolution of the detailed timescale of metamorphism, which is required to constrain tectonic models.

We investigate the timing of metamorphism in the Nyalam transect, for which crucial structural kinematics, metamorphic conditions and *P–T* paths have already been determined (Liu *et al.*, 2012; Larson, 2012; Larson *et al.*, 2013; Wang *et al.*, 2013, 2015), but geochronology is still lacking. Ten samples of different metamorphic grade were investigated for monazite U–Pb dating, internal zoning, mineral inclusions and trace element signatures. The metamorphic conditions of monazite formation were constrained by comparison with garnet trace element zoning. Rutile U–Pb ages were obtained for the first time in the GHC metapelites to constrain the timing of cooling in a subset of samples, whereas Zr-in-rutile temperatures were determined to retrieve peak temperature conditions. The results give new insights into the tectonic evolution of the GHC, particularly the issue of whether propagating thrusting or partial melting dominates the exhumation of high-grade metamorphic rocks in the Himalayan orogen.

GEOLOGICAL SETTING

The Himalayan orogen is commonly divided from north to south into the Tethyan Himalayan Sequence (THS), GHC, Lesser Himalayan Sequence (LHS) and Siwalik Group (SG) by four first-order tectonic boundaries that run ~2500 km along the strike of the orogen (Fig. 1a; Yin, 2006). These tectonic boundaries are the top-to-north STD and the top-to-south MCT, Main Boundary Thrust (MBT) and Main Frontier Thrust (MFT). The MCT thrust the amphibolite- to granulite-facies GHC rocks on top of the greenschist- to lower amphibolite-facies LHS rocks (e.g. Le Fort, 1975; Arita, 1983; Schelling, 1992; Pearson & DeCelles, 2005; Searle *et al.*, 2008; Larson *et al.*, 2013). The STD separates the fossiliferous sediments of the THS from the underlying GHC (e.g. Burchfiel & Royden, 1985; Burchfiel *et al.*, 1992; Searle *et al.*, 2003; Cottle *et al.*, 2007).

The Nyalam region in the central Himalaya is located ~50 km to the east of the well-studied Langtang region (Fig. 1a) and exposes similar metamorphic rocks (Reddy *et al.*, 1993; Fraser *et al.*, 2000; Kohn *et al.*, 2004). Typical lithologies include graphite-rich pelitic schists and Neoproterozoic granitic orthogneisses in the LHS, and migmatitic paragneisses, calc-silicate interlayers and Early Paleozoic granitic orthogneisses in the GHC (Schelling, 1992; Larson, 2012; Wang *et al.*, 2013; Larson *et al.*, 2013). Foliations in the GHC rocks generally have moderate dips towards N5–30°W or N5–20°E (Fig. 1b). Despite the debate on the position of the MCT in other Himalayan transects [see review by Searle *et al.* (2008)], the MCT in this section was mapped at the top of the Melung–Salleri orthogneiss and staurolite-bearing schist, based on the presence of a metamorphic and geochronological discontinuity (Larson *et al.*, 2013). The hanging-wall rocks (GHC) experienced a clockwise *P–T* path with a kyanite-grade metamorphic peak at ~19 Ma, whereas the footwall rocks (MCT zone and LHS) record a hairpin-type *P–T* path with a staurolite–kyanite grade metamorphic peak at ~10–8 Ma (Larson *et al.*, 2013). The STD has been recognized ~30 km north of Nyalam town and is characterized by a 3 km wide ductile shear zone and decreasing metamorphic grade from amphibolite to greenschist facies (Liu *et al.*, 2012; Myrow *et al.*, 2009; Wang *et al.*, 2013). Timing of movement along the STD was constrained to be ~27–14 Ma by cross-cutting leucogranite dykes (Liu *et al.*, 2012; Wang *et al.*, 2013).

A typical Barrovian-type metamorphic zonation has been recognized across the LHS and GHC. Metamorphic grade gradually increases toward higher structural levels (Fig. 1b) from chlorite, garnet and staurolite–kyanite grade in the LHS, to sillimanite–muscovite, sillimanite–K-feldspar and cordierite grade in the GHC (Larson, 2012; Wang *et al.*, 2013). Results from garnet–biotite Fe–Mg exchange thermometers show that minimum peak temperature conditions gradually increase from ~580°C in the upper LHS to ~750°C in the upper GHC, whereas metamorphic pressures decrease from 10–13 kbar to 4–7 kbar towards higher structural levels (Wang *et al.*, 2013). Melt is absent in the LHS metapelitic rocks, but segregations of leucosome are abundant across the GHC. Generally, the amount of melt production increases with increasing temperature and decreasing pressure through a series of melting reactions: (1) H_2O-saturated melting ($Ms + Ab + Qz + H_2O = melt$; Imayama *et al.*, 2010; Wang *et al.*, 2015; mineral abbreviations according to Whitney & Evans, 2010) dominated in the kyanite and sillimanite–muscovite zones; (2) dehydration melting of muscovite ($Ms + Pl + Qz = Kfs + Als + melt$; Imayama *et al.*, 2010; Groppo *et al.*, 2012) dominated in the sillimanite–K-feldspar zone; (3) dehydration melting of biotite producing garnet ($Als + Bt + Pl + Qz = Grt + Kfs + melt$, Groppo *et al.*, 2012) or cordierite ($Als + Bt + Pl + Qz = Crd + Kfs + melt$, Groppo *et al.*, 2013) also occurred in some of the higher grade rocks.

A few studies have investigated the discontinuities within the GHC in this transect. Early work suggested several thrusts (Ishida, 1969; Ishida & Ohta, 1973), but later studies have shown that the entire GHC experienced penetrative deformation and that the previously proposed thrusts lack structural evidence (Larson, 2012). The Nyalam Discontinuity was recognized within the sillimanite–K-feldspar zone of the GHC based on an inversion in *P–T* conditions of ~40°C and ~3 kbar toward higher structural levels (Fig. 1b; Wang *et al.*, 2013). It is located at a similar structural level to the adjacent 'Langtang Thrust', which is marked by a discontinuity in *P–T* conditions and monazite Th–Pb ages (Kohn *et al.*, 2004; Kohn, 2008). In this study, the GHC is divided into the lower and upper blocks by the Nyalam Discontinuity and Langtang Thrust.

SAMPLE DESCRIPTION

Nine samples of migmatitic metapelite or metapsammite were collected along a north–south transect

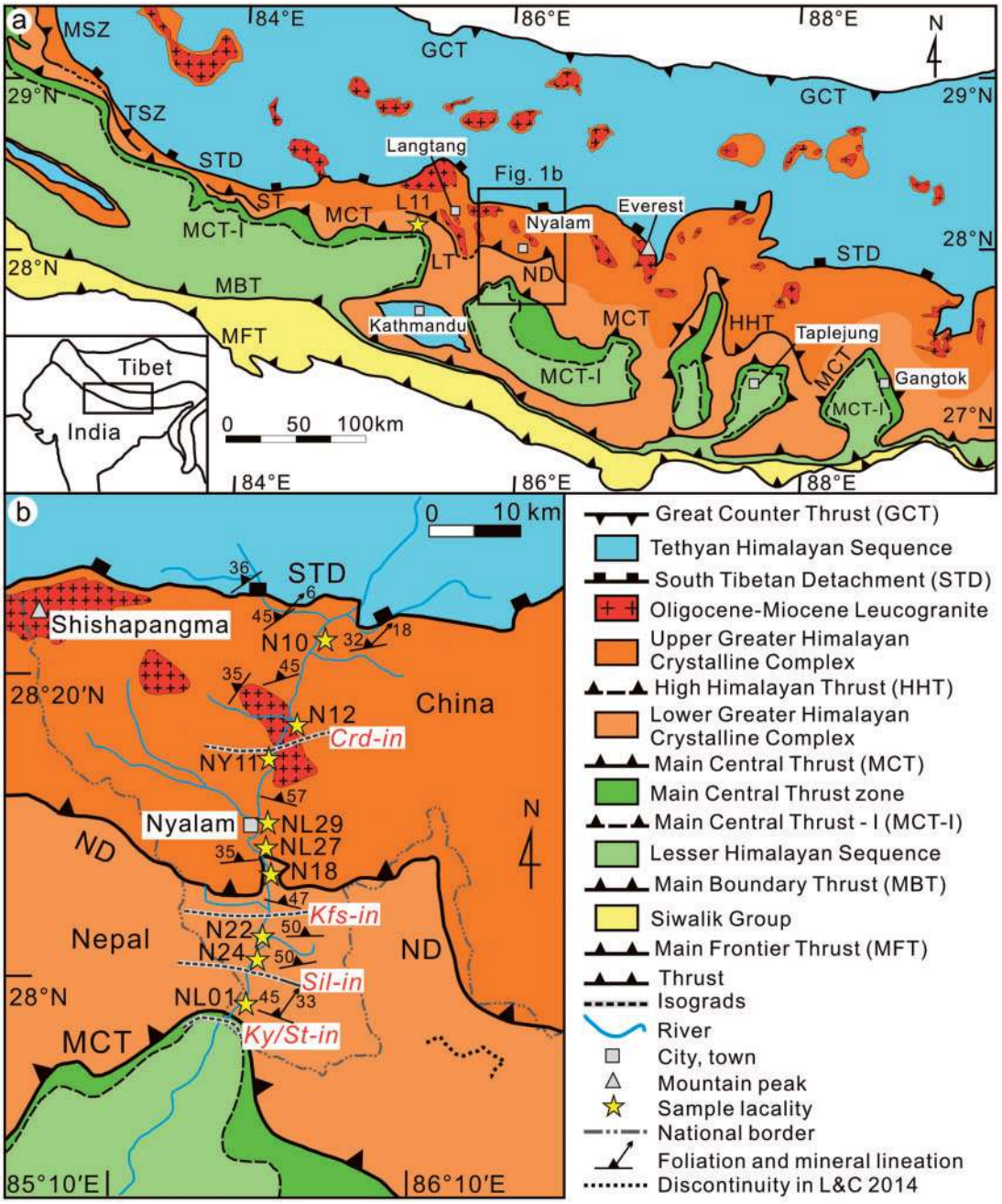

Fig. 1. (a) Geological map of the central Himalaya highlighting the lithostratigraphic units and main structures [modified after Yin (2006)]. The High Himalayan Thrust (HHT) is inferred from this study. Inset map shows the location. (b) Detailed geological map of the Nyalam region showing sample locations and metamorphic isograds [modified after Searle *et al.* (1997) and Wang *et al.* (2013)]. Abbreviations for local structures (see text for details): MSZ: Mangri shear zone; TSZ, Toijem shear zone; ST, Sinuwa thrust; LT, Langtang Thrust; ND, Nyalam Discontinuity; HHT, High Himalayan Thrust. Mineral abbreviations follow Whitney & Evans (2010). L&C 2014, Larson & Cottle (2014).

through the GHC in the Nyalam region (Fig. 1b). Of these, four samples were located structurally below the Nyalam Discontinuity and five samples were collected structurally above it. An additional metapelitic sample (L11) is from the Langtang region, and was collected from structurally below the Langtang Thrust within the kyanite zone defined by Kohn (2008) (Fig. 1a). Sample global positioning system (GPS) locations, mineral assemblages and *P–T* estimates are given in Table 1. *P–T* estimates for the same or adjacent samples from the Nyalam transect were obtained by Wang *et al.* (2013) using the garnet–biotite thermometer, garnet–Al_2SiO_5–quartz–plagioclase barometer and garnet–biotite–plagioclase–quartz barometer. Mineral compositions and the *P–T* calculation method for sample L11 are given in Supplementary Data (SD) Electronic Appendix A (supplementary data are available for downloading at http://www.petrology.oxfordjournals.org).

Table 1: Locations, mineral assemblages and P–T conditions of studied samples

Sample	Locality	GPS coordinates	Rock type	Main minerals	Accessory minerals	Retrogression	Melting degree (%)	Melting reaction	*P* at peak *T* (kbar)	Peak *T* (°C)	Zr-in-rutile *T* (°C)
NL01	Lower GHC, Nyalam	27°58′8·39″N, 85°58′2·97″E	Migmatitic metapelite	Grt(~3%), Bt, Ms, Pl, Ky, Qz	Mnz, Ap, Zr, Rt		5 ± 2	H_2O-saturated	9·9 ± 0·8	652 ± 25	640 ± 35
L11	Lower GHC, Langtang	28°13′3·00″N, 85°21′23·60″E	Migmatitic metapelite	Grt(~3%), Bt, Ms, Pl, Ky, Qz	Mnz, Ap, Zr, Rt		5 ± 2	H_2O-saturated	12·4 ± 0·8	673 ± 25	659 ± 35
N24	Lower GHC, Nyalam	28°2′30·39″N, 85°59′18·28″E	Migmatitic metapelite	Grt(~1%), Bt, Ms, Pl, Sil(f), Qz	Mnz, Ap, Zr		7 ± 3	H_2O-saturated	7·3 ± 0·8 (NL07)	639 ± 25 (NL07)	655 ± 35 (NL07)
N22	Lower GHC, Nyalam	28°3′6·90″N, 85°59′39·24″E	Orthogneiss	Grt(~1%), Bt, Ms, Pl, Qz	Mnz, Ap, Zr		~0	No	6·1 ± 0·8 (NL16)	651 ± 25 (NL16)	675 ± 36 (NL16)
N18	Lower GHC, Nyalam	28°7′20·64″N, 85°59′29·90″E	Migmatitic metapelite	Grt(~3%), Bt, Kfs, Pl, Sil, Qz	Mnz, Ap, Zr	Chl	20 ± 5	Ms dehydration	3·9 ± 0·8	669 ± 25	
NL27	Upper GHC, Nyalam	28°8′0·43″N, 85°58′25·65″E	Migmatitic metapelite	Grt(~5%), Bt, Kfs, Pl, Sil, Qz	Mnz, Ap, Zr	Ms	15 ± 5	Ms dehydration	6·7 ± 0·8	713 ± 25	
NL29	Upper GHC, Nyalam	28°8′28·59″N, 85°58′54·56″E	Migmatitic metapelite	Bt, Kfs, Pl, Sil, Qz	Mnz, Ap, Zr		20 ± 5	Ms dehydration			
NY11	Upper GHC, Nyalam	28°12′3·31″N, 85°59′21·71″E	Migmatitic metapsammite	Bt, Kfs, Pl, Qz	Mnz, Ap, Zr, Rt		25 ± 5	Ms dehydration	4·1 ± 1·2 (NL33)	749 ± 50 (NL33)	730 ± 40
N12	Upper GHC, Nyalam	28°13′2·62″N, 86°0′1·13″E	Migmatitic metapsammite	Bt, Kfs, Pl, Qz	Mnz, Ap, Zr, Rt	Ms, Pl + Bt symplectite	25 ± 5	Ms dehydration	4·1 ± 1·2 (NL33)	749 ± 50 (NL33)	747 ± 41
N10	Upper GHC, Nyalam	28°20′7·86″N, 86°3′10·34″E	Migmatitic metapsammite	Grt(~7%), Bt, Kfs, Pl, Qz	Mnz, Ap, Zr		20 ± 5	Ms/Bt dehydration	6·9 ± 1·2	726 ± 50	

f, fibrolite sillimanite. Degree of partial melting was defined by textures and amount of leucosome in the samples. *P–T* conditions of the same samples from the Nyalam transect have been published by Wang *et al.* (2013) using the garnet–biotite thermometer, garnet–Al_2SiO_5–quartz–plagioclase barometer and garnet–biotite–plagioclase–quartz barometer. *P–T* conditions of samples N24, N22, NY11 and N12 are from adjacent samples of Wang *et al.* (2013) (sample numbers given). Mineral compositions and *P–T* calculation methods for sample L11 are listed in Supplementary Data Electronic Appendix A. Zr-in-rutile temperatures were calculated using the Tomkins *et al.* (2007) thermometer and the listed pressures were used for correction in each sample.

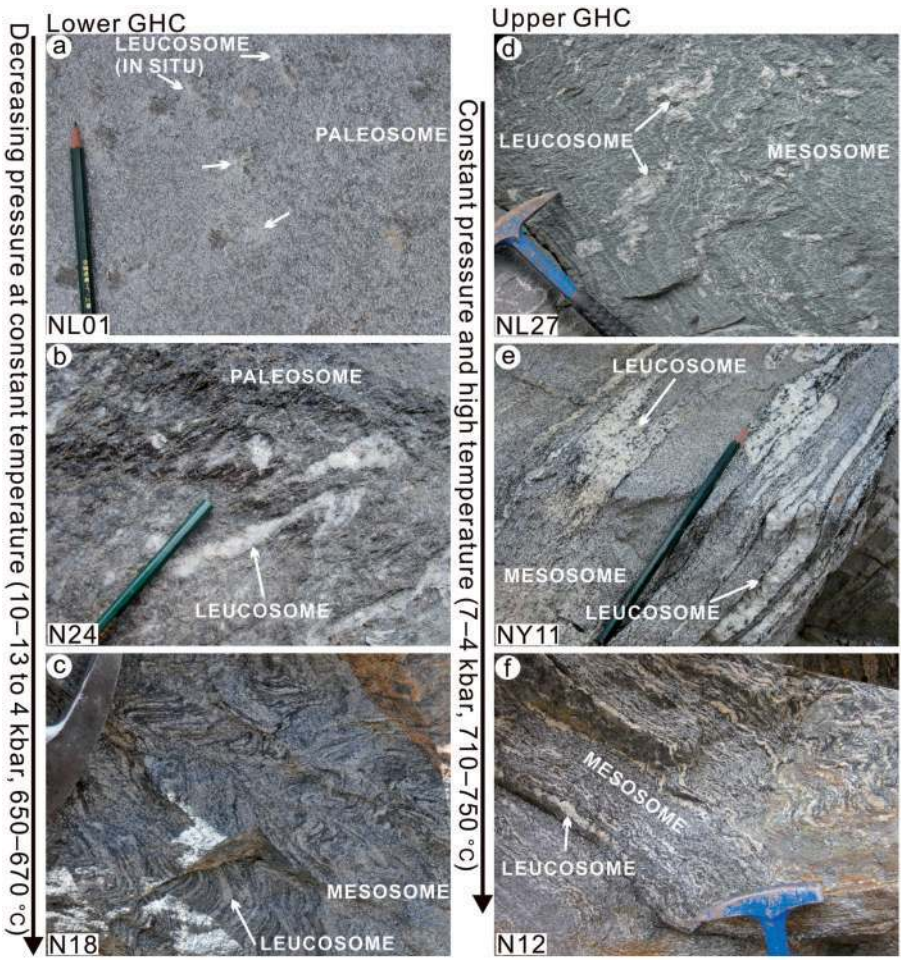

Fig. 2. Outcrop photographs of migmatites from the Greater Himalayan Crystalline (GHC) sequence, Nyalam, central Himalaya. The images highlight the degree of partial melting (defined by textures and amount of leucosome). (a) Incipient melting (5 ± 2%, NL01) in the lower GHC: pockets of melts crystallized *in situ* within the paleosome. (b) Low-grade partial melting (7 ± 3%, N24) in the lower GHC with segregations of leucosome enclosed by paleosome. (c) High-grade partial melting that resulted from decompression (~4 kbar and ~670°C, 20 ± 5%, N18) in the lower GHC, with segregations of leucosome enclosed by mesosome. Former melt is pervasively distributed and a syn-anatectic flow structure is dominant. (d) Medium-grade partial melting (15 ± 5%, NL27) in the upper GHC. (e) Pervasive partial melting during high-temperature metamorphism (~750°C, 25 ± 5%, NY11) in the upper GHC. This image was modified from Wang *et al.* (2013), with kind permission from John Wiley and Sons. (f) High-grade partial melting (25 ± 5%, N12) in the upper GHC with clear syn-anatectic flow structures.

Lower GHC samples

Most samples from the lower GHC have a metatexite migmatite texture (Sawyer & Brown, 2008), with degree of partial melting—as defined by textures and amount of leucosome—increasing toward the north. In the outcrops from which samples NL01 and L11 were taken, paleosome (part of the migmatite that shows no evidence of melting) constitutes the majority of the rock (>95%) and no flow structure was observed (Fig. 2a). Leucosome forms millimeter-scale pockets (5 ± 2%), which are common around garnet porphyroblasts. In sample N24, centimeter-scale leucosome segregations (7 ± 3%) are visible, but the paleosome still dominates in volume (>90%, Fig. 2b). Sample N18 has a higher percentage of leucosome (20 ± 5%), which forms centimeter-scale quartzo-feldspathic layers or pods (Fig. 2c). Sample N22 is referred to as orthogneiss, because it is more felsic-rich (>70%, Fig. 3d) and does not contain an aluminium-silicate phase, and the inherited monazite population in this sample yields a single age group (see below). Partial melting is not obvious in sample N22. Samples NL01, L11 and N24 were intentionally collected to represent the paleosome portion of the outcrop, whereas sample N18 is a mesosome as in this outcrop the segregations of leucosome cannot be avoided at the scale of the sample.

Estimates of peak temperature conditions are similar across the lower GHC samples (640–670°C), but the equilibrium pressure conditions at peak temperature decrease toward the north from 13–10 to ~4 kbar (Wang *et al.*, 2013). Specifically, samples NL01 and L11 are in the kyanite–muscovite field, sample N24 is in the sillimanite–muscovite field and sample N18 represents the sillimanite–K-feldspar field (Fig. 3; Table 1). All samples contain plagioclase, quartz, biotite, an aluminum-silicate phase and garnet. Muscovite is in equilibrium at

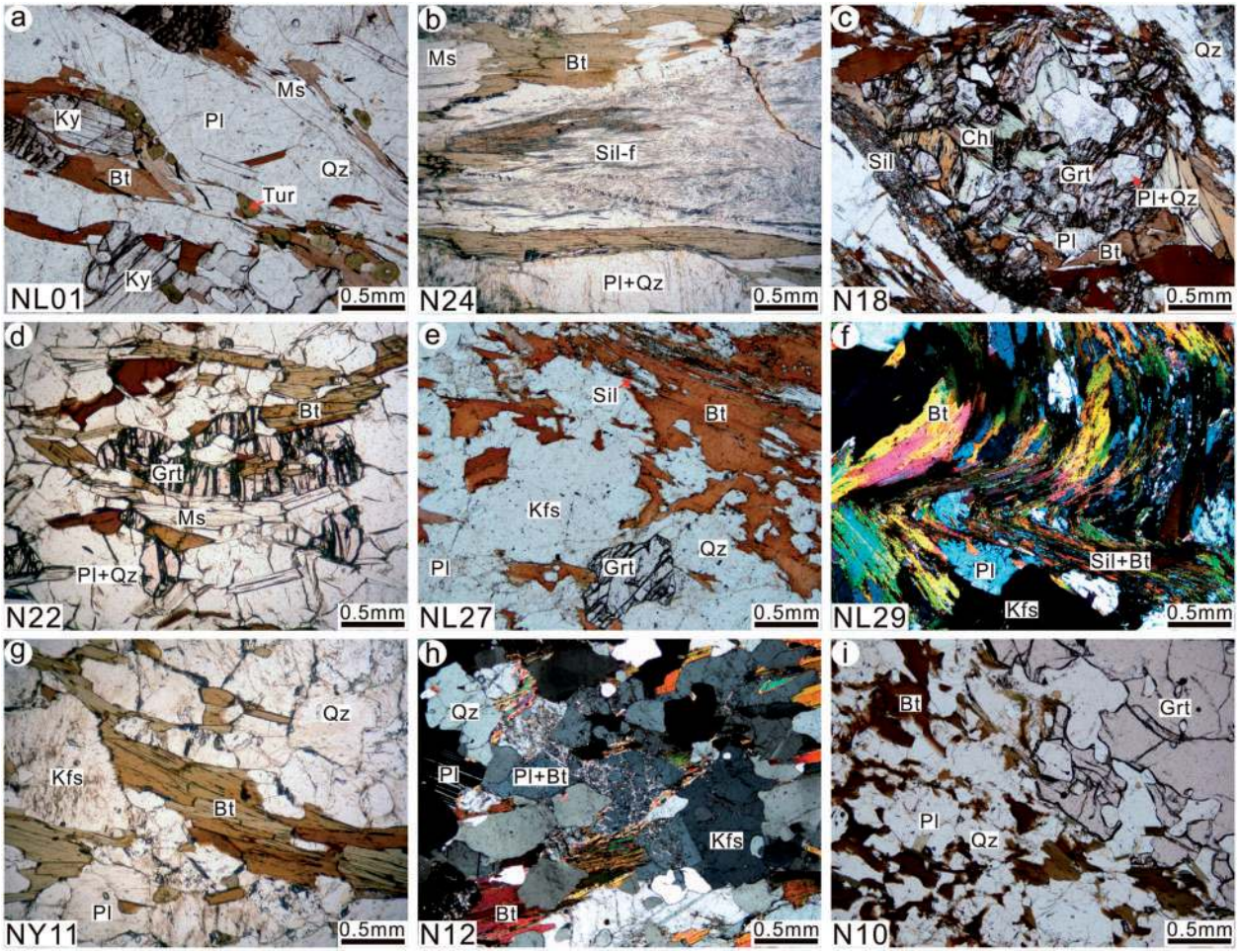

Fig. 3. Photomicrographs of thin sections of investigated samples. (a) Typical kyanite-zone metapelitic assemblage with abundant kyanite coexisting with muscovite. (b) Fibrolite sillimanite aligned with biotite, formed by consumption of muscovite. (c) Replacement of garnet by biotite, sillimanite, quartz and plagioclase via decompression. Chlorite replaced garnet during retrogression. (d) Orthogneiss sample that contains abundant quartzo-feldspathic domains and a few garnet grains. (e) Typical high-temperature metapelitic assemblage with prismatic sillimanite and K-feldspar, and lack of muscovite. (f) Folded prismatic sillimanite and biotite. Crossed polars. (g) High-temperature metapsammite sample with a simple assemblage of K-feldspar, plagioclase, biotite and quartz. (h) High-temperature metapsammite sample with retrograde symplectite of plagioclase and biotite. (i) Peritectic garnet formed through dehydration of biotite.

peak stage in samples NL01, L11, N24 and N22, but is absent in sample N18. The above mineral assemblages indicate that partial melting was the result of H_2O-saturated melting in samples NL01, L11 and N24, but of muscovite dehydration melting in sample N18. Garnet is present in all the lower GHC samples, albeit in small volumes (1–3%). Polymineralic inclusions in garnet that have negative crystal shapes (i.e. Pl + Qz inclusion in Fig. 3c) increase in size from 5 to 100 μm with increasing structural level. These inclusions are considered to have crystallized from previous melt pores (nanogranite; Ferrero *et al.*, 2012; Groppo *et al.*, 2012; Wang *et al.*, 2015). Most of the samples show no sign of retrograde metamorphism other than occasional fractures filled by retrograde chlorite or resorbed garnet rims in sample N18. All the samples contain accessory monazite, zircon and apatite, whereas rutile occurs only in samples NL01 and L11, and is in textural equilibrium with kyanite.

Upper GHC samples

Most samples from the upper GHC have a higher content of leucosome than samples from the lower block, resulting in a diatexite migmatite texture (Sawyer & Brown, 2008). In all samples leucosome is widely distributed and the sample is a mix of leucosome and residuum (mesosome). Leucosome segregations can reach decimeter-scale and are usually enclosed by mesosome (Fig. 2d–f). The rocks are dominated by syn-anatectic flow structures. In samples NL27, NL29 and N10, leucosome makes up about 15–20% of the rock, whereas samples NY11 and N12 have a higher percentage of leucosome (25 ± 5%). The samples used for geochronology were collected from the mesosome portion but still contain small segregations of leucosome.

Estimated peak temperature conditions for the upper GHC samples are similar at 710–750°C; equilibrium pressures at the peak temperatures decrease toward the north from 7 to 4 kbar (Wang *et al.*, 2013). Most

samples represent the sillimanite–K-feldspar stability field and contain K-feldspar, biotite, plagioclase, quartz or sillimanite, which indicates that partial melting was mainly produced by muscovite dehydration melting. Sillimanite is present only in pelitic samples NL27 and NL29 (Fig. 3e and f), and garnet occurs only in samples NL27 and N10 (Fig. 3e and i) as inclusion-free porphyroblasts. In sample N12, a retrograde symplectite of plagioclase and biotite partly replaces the prograde minerals (Fig. 3h). Corroded biotite crystals are partly consumed to form K-feldspar and peritectic garnet in sample N10 (Fig. 3i), which indicates that dehydration melting of biotite also occurred. All the samples contain accessory monazite, zircon, and apatite; rutile is present only in samples NY11 and N12, which record slightly higher temperatures and lower pressures.

METHODS

Monazite and rutile crystals were separated using standard heavy liquid and magnetic techniques, and handpicked under a binocular microscope. The grains were then mounted in epoxy resin and polished to expose the grain centers. Back-scattered electron (BSE) images of monazite and rutile were produced with a JEOL JSM-6610 A scanning electron microscope at the Australian National University (ANU), with working conditions of 15 kV, 60 μA and ~10 mm working distance. Inclusions in monazite were identified by a JED-2300 energy-dispersive X-ray system installed on the same instrument. Transmitted and reflected light images of monazite and rutile were also used to avoid inclusions and fractures during analysis

SHRIMP U–Th–Pb

U, Th and Pb analyses of monazite were performed by sensitive high-resolution ion microprobe (SHRIMP II and SHRIMP RG) at ANU. Instrumental conditions and data acquisition were generally as described by Williams (1998). Energy filtering was applied (Rubatto *et al.*, 2001) to eliminate the interference on ^{204}Pb, reduce the high counts on the ThO peak, and suppress any matrix effect. A matrix effect for monazite reported by Fletcher *et al.* (2010) was not observed in this study (SD Electronic Appendix Fig. 1). The data were collected in sets of six scans throughout the masses with a spot size of 20–30 μm and reference material was analyzed at each third analysis. The measured ^{206}Pb/^{238}U ratio was corrected using reference monazite Delaware 44069 (425 Ma; Aleinikoff *et al.*, 2006). In most of the analytical sessions, calibration errors were <2·8% (2σ, seven samples), but were slightly larger (3·5–3·7%, 2σ) in some sessions (three samples); in each case the calibration error was propagated to the single analyses. For the analyses yielding Cenozoic ages, the data were corrected for common Pb based on the measured ^{207}Pb/^{206}Pb (by assuming concordance), whereas the pre-Cenozoic inherited ages were corrected using the measured ^{204}Pb (Williams, 1998). The analyses used for average age calculations have a small percentage of common Pb (mostly <1%, few 2–5%). The common Pb compositions predicted by the Stacey & Kramers (1975) model were used ($^{207}Pb_c/^{206}Pb_c = 0{\cdot}837 \pm 0{\cdot}042$, for Himalayan ages). For the rim analyses of sample N22, which are particularly rich in initial Pb, the initial Pb composition was obtained from the Y-intercept of a free regression in the uncorrected Tera–Wasserburg plot ($^{207}Pb_c/^{206}Pb_c = 0{\cdot}511 \pm 0{\cdot}026$). This composition deviates significantly from the model common Pb and recalculating the age with this input is a more accurate approach. The software Squid 1 and Isoplot/Ex (Ludwig, 2008) were used for data reduction and age calculation, and the ^{238}U, ^{235}U and ^{232}Th decay constants of Steiger & Jäger (1977) were used. Average U–Pb ages are quoted at the 95% confidence level. Analytical U–Th–Pb data are listed in SD Electronic Appendix Table 1.

For Th-rich minerals such as monazite, excess ^{206}Pb owing to decay of ^{230}Th can lead to overestimation of the real age. This problem has been reported for Himalayan leucogranite (Schärer, 1984), where the melt may be rich in ^{230}Th. However, for Himalayan metapelites and metapsammites, the presence of excess ^{206}Pb is less obvious and Th–Pb ages are usually in agreement with U–Pb ages (Martin *et al.*, 2007; Rubatto *et al.*, 2013; Stearns *et al.*, 2013; Larson & Cottle, 2014). For most analyses in this study, Th–Pb ages are in agreement with U–Pb ages within 2σ uncertainties and no correlation was observed between U–Pb age and Th/U ratios (SD Electronic Appendix Fig. 2a–d). The SHRIMP set-up is best suited for measuring the lower count rates of Pb, and is less reliable when measuring very high count rates, such as those for Th in monazite. For these reasons, we consider U–Pb ages more accurate and prefer them to Th–Pb ages. An exception is made for samples N18 and N12, for which U–Pb ages are 1–3 Myr older than Th–Pb ages and could be affected by excess ^{206}Pb (SD Electronic Appendix Fig. 2e–h). For these two samples, the ages were reported as a range considering the average U–Pb and Th–Pb ages.

LA-ICP-MS trace elements

Trace element analyses of monazite, rutile and garnet were obtained by a laser ablation–inductively coupled plasma–mass spectrometry (LA-ICP-MS) at ANU, using a pulsed 193 nm ArF Excimer laser with 100 mJ energy at a repetition rate of 5 Hz (Eggins *et al.*, 1998) coupled to an Agilent 7700 quadrupole ICP-MS system. Most LA-ICP-MS analyses of monazite were performed on the same site as the 2 μm deep SHRIMP pits. Garnet was analyzed in polished thin sections, whereas monazite and rutile were mounted in epoxy disks. Spot sizes of 28 μm (monazite) and 47 μm (rutile and garnet) were used and reference material was analyzed each tenth analysis. External calibration was performed relative to NIST 610 glass (rutile) or NIST 612 glass (monazite and garnet) and internal standardization was based on

stoichiometry of Ce for monazite (23·6 wt %), Ti for rutile (59·93 wt %) and Si for garnet (17·76 wt %). Accuracy and precision of the analyses were evaluated with a BCR-2G secondary glass standard and are always better than 10% combined. Analyses that have apparent contamination from inclusions or those with insufficient data collecting duration (<10 s) were discarded. Trace element data reduction was performed using the software lolite v.2.5 (Paton *et al.*, 2010). Analytical data are listed in SD Electronic Appendix Tables 2, 3 and 4. Rare earth element (REE) patterns of monazite and garnet were normalized to chondrite (McDonough & Sun, 1995).

Zr-in-rutile temperatures were calculated using the calibration of Tomkins *et al.* (2007) for the β-quartz field. The pressures used for correction for each sample were from Wang *et al.* (2013) and are listed in Table 1. For comparison, calculated results using the calibration of Watson *et al.* (2006), which assumes a constant pressure of 10 kbar, are also listed in SD Electronic Appendix Table 4. Generally, differences in temperature calculated using different calibrations are less than ±30°C. Uncertainties are calculated by considering a conservative analytical error of ±15% in Zr measurements, ±0·8 kbar (or ±1·2 kbar) for pressure estimates and a ±3% (±20°C) propagated uncertainty from the calibration of the thermometer. The activities of Si and Zr are fully buffered, as all the metasedimentary samples in this study are rich in quartz and zircon. The 47 μm laser pit was always located at the center of the grains to avoid possible complications from Zr diffusion at the rim during cooling.

LA-ICP-MS U–Pb

U–Pb analyses of rutile were performed with the same LA-ICP-MS system and working conditions as the trace element analyses. A large spot size of 62 μm and a long dwell time (70–90 ms) for ^{206}Pb, ^{207}Pb, ^{208}Pb, ^{232}Th and ^{238}U were used to improve precision. Each analysis measures the background for ~30 s before switching on the laser for ~40 s. Reference material was analyzed each fifth analysis. The measured ^{206}Pb/^{238}U ratio was corrected using reference rutile Wodgina-B (2846 Ma; isotope dilution thermal ionization mass spectrometry data; Ewing, 2011). Data reduction, including corrections for baseline, instrumental drift, mass bias and downhole fractionation, was performed using the software lolite version 2.5 (Paton *et al.*, 2010). The analyzed rutile samples usually have a very low Th content (Th/U generally < 0·001), which is an ideal case for common Pb correction using the measured ^{206}Pb/^{208}Pb (Zack *et al.*, 2011). The fraction of common ^{206}Pb (f_c) is calculated from a given common Pb composition (^{206}Pb$_c$/^{208}Pb$_c$) by assuming Th/U ≈ 0:

$$f_c(^{206}\mathrm{Pb}) = (^{206}\mathrm{Pb}_m/^{208}\mathrm{Pb}_m)/(^{206}\mathrm{Pb}_c/^{208}\mathrm{Pb}_c).$$

For Himalayan samples, the present ^{206}Pb$_c$/^{208}Pb$_c$ ratio of 0·484 ± 0·024 was used (Stacey & Kramers, 1975). To ensure accuracy, only those analyses with common Pb fraction (f_c) of less than 8% and U concentrations higher than 40 ppm were used for average age calculation. Uncertainties of f_c(^{206}Pb) were calculated using the formula suggested by Gregory *et al.* (2007) by considering the uncertainties in estimating the ^{206}Pb$_c$/^{208}Pb$_c$ composition (±5%) and uncertainties on the measured ^{206}Pb$_m$/^{208}Pb$_m$ ratios. Uncertainties on the corrected ^{206}Pb/^{238}U ratio are quoted at the 2σ level and were calculated using the formula suggested by Andersen (2002) by considering the analytical errors, propagated calibration errors of the standard and errors from common Pb correction. U–Th–Pb data are listed in SD Electronic Appendix Table 5. Owing to the young ages and little accumulation of radioactive ^{207}Pb, the obtained ^{207}Pb/^{235}U ages are less reliable than the ^{206}Pb/^{238}U ages. Therefore, only the ^{206}Pb/^{238}U ages were reported. Total ^{238}U/ ^{206}Pb–^{207}Pb/ ^{206}Pb Tera–Wasserburg plots are included in SD Electronic Appendix Fig. 7.

MONAZITE U–PB GEOCHRONOLOGY AND TRACE ELEMENTS

Most monazite grains are clear, light yellow or yellow in color, and euhedral in shape. Monazite in lower grade sample NL01 has a relatively small size (<60 μm in diameter), whereas monazites in higher-grade samples NY11 and N12 are usually larger than 300 μm in diameter. Internal zoning of monazite is described according to the high-contrast BSE images (Figs 4 and 5); this is a reflection of the total Z number. Average ^{206}Pb/^{238}U ages are reported according to the statistically consistent groups ($n \geq 5$). Whenever the mean square of weighted deviates (MSWD) is above the threshold of two, a range of dates is reported. U–Pb analyses uncorrected for common Pb are presented in Tera–Wasserburg plots (Figs 4 and 5) and corrected ages are shown in probability diagrams (SD Electronic Appendix Fig. 3). Trace element compositions of dated monazite are reported with particular emphasis on the features distinguishing different domains or statistically consistent age groups (Figs 6 and 7; SD Electronic Appendix Fig. 5). Monazite inclusions, ages and relevant trace element signatures are summarized in Table 2.

Lower GHC samples

In metapelites NL01, N24 and N18, monazites have irregular cores, which are exposed only in some grains, and which are cut across by BSE-dark rims (Fig. 4a–c). In sample NL01, cores yield an average age of 18·6 ± 0·6 Ma (MSWD 1·9, *N* 5/6), whereas rims (including unzoned crystals) yield younger ages of 16·1–13·7 Ma, with a cluster at 14·1 ± 0·4 Ma (MSWD 1·6, *N* 6/10). However, in samples N24 and N18, core and rim ages cannot be resolved with the present analytical precision and yield single peaks at 17·3 ± 0·2 Ma (MSWD 1·9, *N* 15/19) and 18·2 ± 0·2 Ma (MSWD 1·6, *N* 22/22),

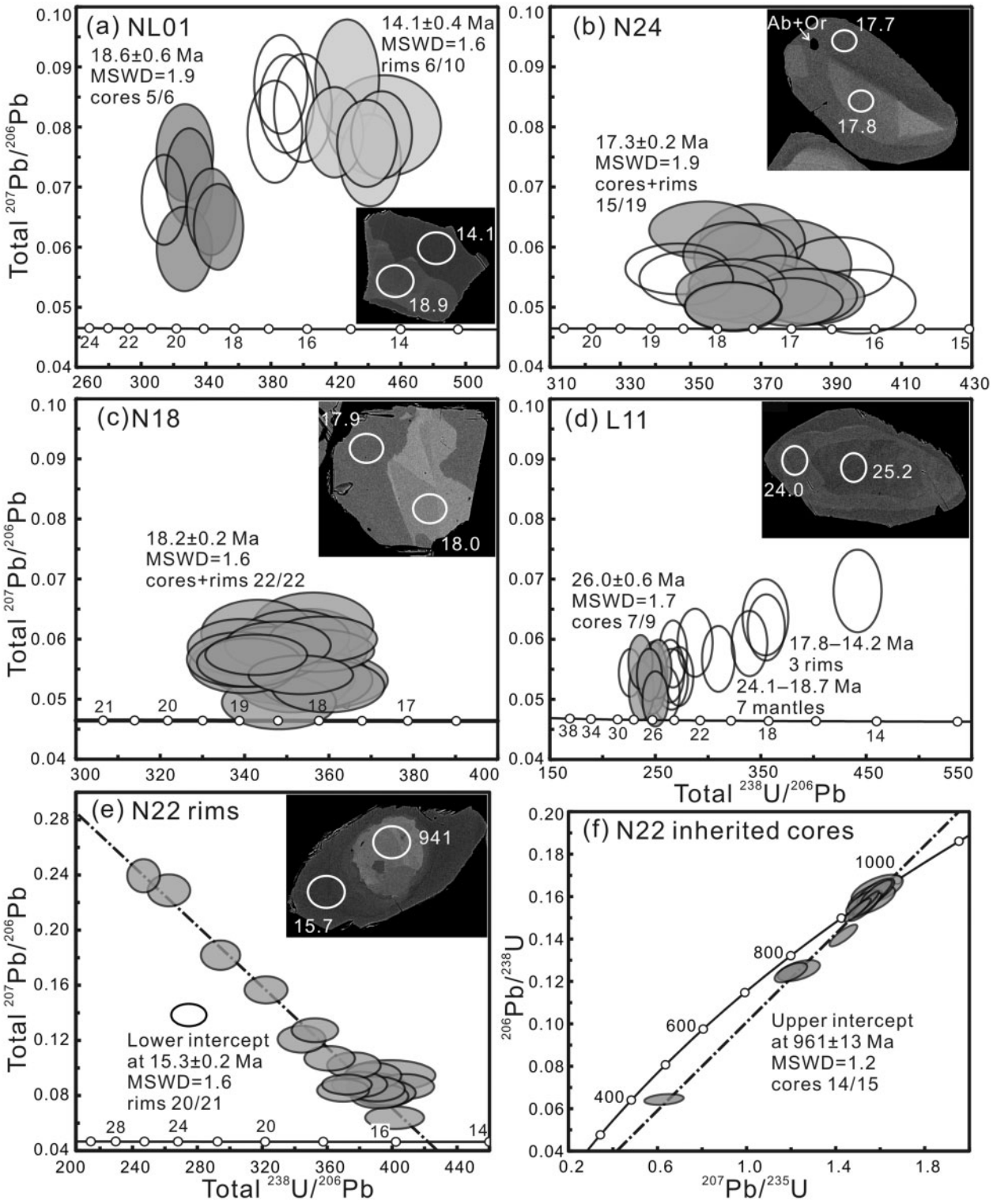

Fig. 4. Representative back-scattered electron images of selected monazite crystals and Tera–Wasserburg diagrams for monazite U–Pb analyses of samples from the lower GHC. Ellipses represent 2σ errors. Only filled gray ellipses were used for average age calculation. Ellipses in the BSE images indicate the location of the SHRIMP analyses and are ~25 μm in diameter; the numbers indicate $^{206}Pb/^{238}U$ ages in Ma. Errors are given in SD Electronic Appendix Table 1.

respectively. Notably, sample N18 may contain excess ^{206}Pb and the U–Pb ages may be overestimated (see details in Methods section). Taking into account the weighted average Th–Pb age (16·7 ± 0·2 Ma, MSWD 1·6, *N* 22/22), we report the age within the range 18·2–16·7 Ma. Monazites in sample N24 contain index mineral inclusions of garnet and aggregates of albite and orthoclase (Fig. 4b), and those in sample N18 contain

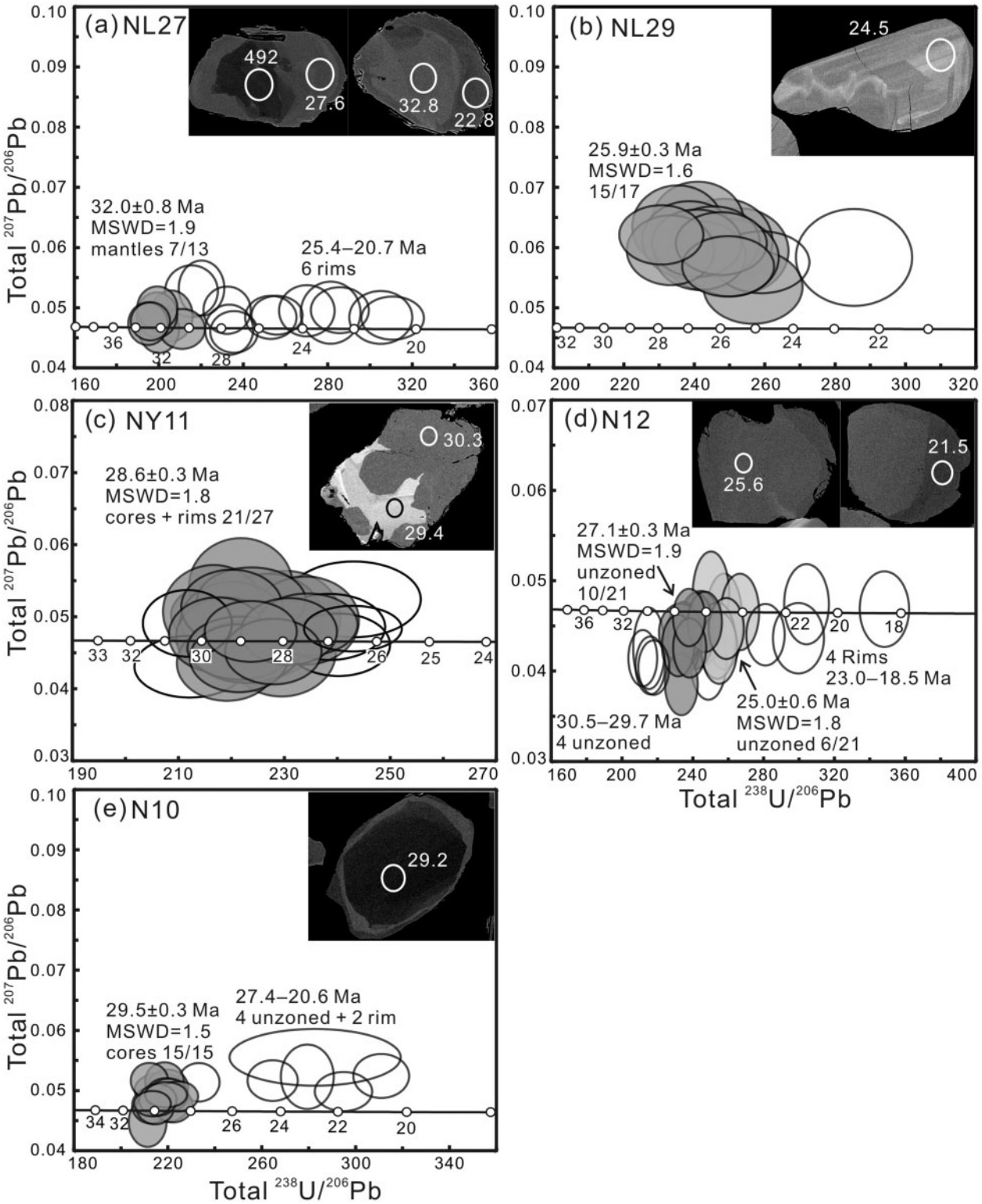

Fig. 5. Representative back-scattered electron images of selected monazite crystals and Tera–Wasserburg diagrams for monazite U–Pb analyses of samples from the upper GHC. Symbols and errors are similar to those of Fig. 4.

garnet, polymineralic inclusions of K-feldspar and quartz and abundant sillimanite (SD Electronic Appendix Fig. 4). Chemically, the rims of sample NL01 are distinctly higher in HREE and Y contents and have lower Gd_N/Lu_N ratios than the cores (Figs 6a and 7a). In sample N24, monazite has a relatively large variation in HREE content, whereas monazite is homogeneous in sample N18 (SD Electronic Appendix Fig. 5a and b). Monazites in sample NL01 have a weak negative Eu anomaly (Eu/Eu* of 0·40–0·44), whereas those of

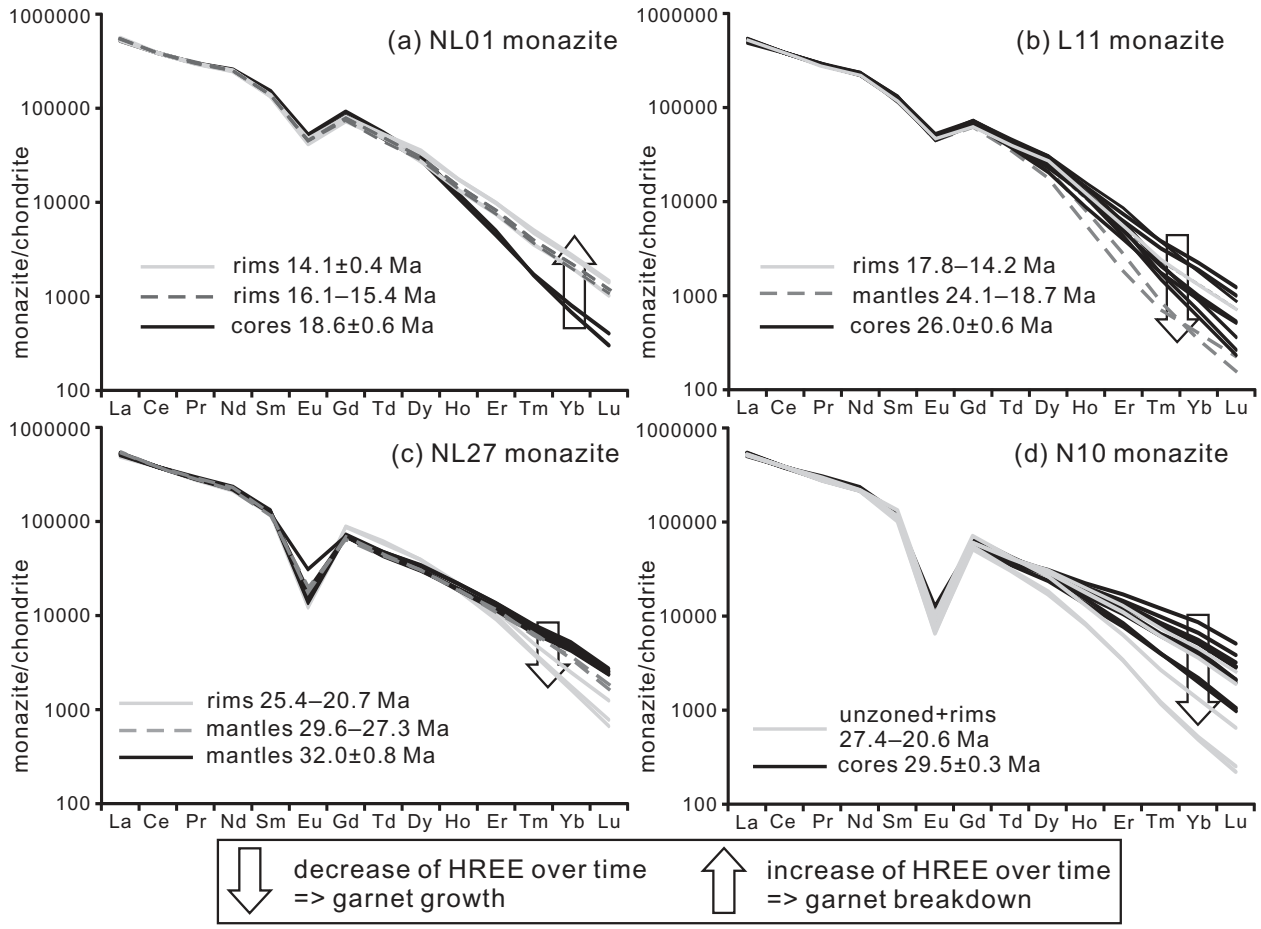

Fig. 6. Chondrite-normalized REE patterns for the dated monazites. The arrows highlight the changes in HREE between different growth zones. Normalizing values are from McDonough & Sun (1995).

samples N24 and N18 have a strong negative Eu anomaly (Eu/Eu* 0·06–0·15).

Orthogneiss N22 contains patchy-zoned monazite cores (Fig. 4e–f) that yield inherited ages with the majority of analyses defining an upper intercept age of 961 ± 13 Ma (MSWD 1·2, *N* 14/15). Rims and unzoned monazite crystals have high fractions of initial Pb (see details in Methods) and yield a lower intercept age of 15·3 ± 0·2 Ma (MSWD 1·6, *N* 20/21). Two core analyses yield intermediate ages of 47–35 Ma, probably owing to some mixing with rim domains. Rims are generally higher in HREE and Y than cores (SD Electronic Appendix Fig. 5c), and show similar negative Eu anomalies (Eu/Eu* 0·16–0·46).

In metapelite L11 from the Langtang transect, most monazites have complex concentric zoning with BSE-dark cores overgrown by a mantle and a thin rim with distinct BSE emission (Fig. 4d). Cores yield an average age of 26·0 ± 0·6 Ma (MSWD 1·7, *N* 7/9), mantle analyses scatter between 24·1 and 18·7 Ma, and three rim analyses give ages of 17·8–14·2 Ma. Inclusions of plagioclase, muscovite, biotite and quartz were observed in cores and mantles. Chemically, cores are higher in HREE and Y than mantles (Figs 6b and 7b). Only one rim could be analyzed for trace elements; it shows the same high HREE and Y contents as the cores. All the analyses have similar weak negative Eu anomalies (Eu/Eu* 0·45–0·52).

Upper GHC samples

In metapelite NL27, a few grains of monazite have small BSE-dark cores and two larger ones were dated at ~492 and 463 Ma (Fig. 5a), whereas three smaller ones (<25 μm) probably yield mixed ages (192, 72, 41 Ma). The ages of the monazite mantles scatter between 33·0 and 25·1 Ma and the only significant peak is at 32·0 ± 0·8 Ma (MSWD 1·7, *N* 7/13). In a few crystals a very narrow (most < 10 μm) rim is present; a single SHRIMP analysis yielded an age of 22·8 ± 0·5 Ma. Unzoned grains that have similar trace element compositions to the rims yield ages scattering between 25·4 and 20·7 Ma. K-feldspar and quartz polymineralic inclusions were observed in the mantles. The mantles dated at ~32·0 Ma are higher in HREE than those dated at 29·6–27·3 Ma, whereas rims and unzoned grains have the lowest HREE contents (Fig. 6c). Mantle or rim analyses exhibit moderate to strong negative Eu anomalies (Eu/Eu* 0·11–0·32).

Most monazites in metapelite NL29 show weak oscillatory zoning or are unzoned (Fig. 5b). They yield a

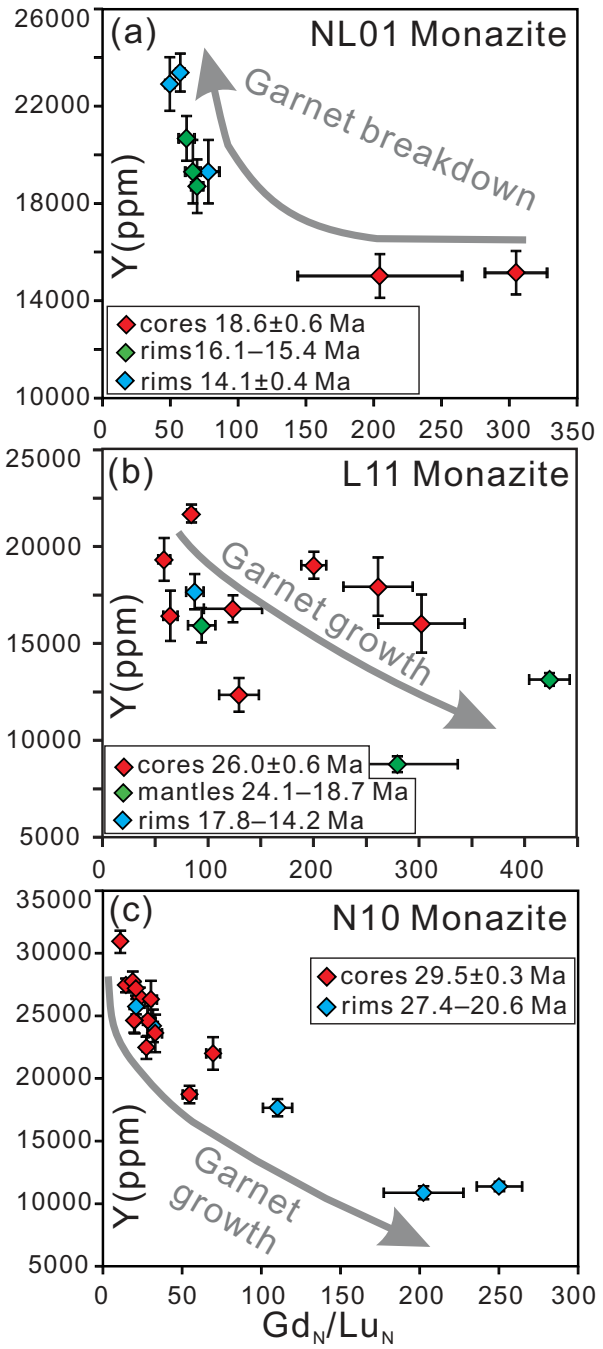

Fig. 7. Y vs Gd_N/Lu_N for dated monazites. The arrows highlight changes in Y and Gd_N/Lu_N values between different growth zones.

single age peak at 25·9 ± 0·3 Ma (MSWD 1·6, *N* 15/17). Monazites in this sample have inclusions of minerals that are stable at peak metamorphic conditions, including sillimanite, biotite, plagioclase, K-feldspar, muscovite and quartz (SD Electronic Appendix Fig. 4). All monazites are homogeneous in HREE and Y contents (SD Electronic Appendix Fig. 5d) and have similar moderate Eu anomalies (Eu/Eu* 0·33–0·41).

In metapsammite NY11, monazite grains exhibit two domains that are intergrown and are distinguished by bright and dark BSE emission (Fig. 5c). The analyses of bright domains have higher Th concentrations (most >70 000 ppm) than the BSE-darker domains (most < 55 000 ppm). Although the overall age is 28·6 ± 0·3 Ma (MSWD 1·8, *N* 21/27, Fig. 6c), some of the brighter domains have a tendency to older ages. The Th-rich domains yield a tight average age of 29·2 ± 0·4 Ma (MSWD 0·3, *N* 9/12), whereas the Th-poor domains yield an average age of 28·4 ± 0·3 Ma (MSWD 1·5, *N* 11/15), which is, however, barely resolvable from the Th-rich domains. Polymineralic inclusions of K-feldspar and quartz are abundant in the Th-poor monazites (SD Electronic Appendix Fig. 4). HREE and Y contents and negative Eu anomalies are similar across both domains (Eu/Eu* 0·12–0·20; SD Electronic Appendix Fig. 5e).

Metapsammite N12 mainly contains unzoned monazite, with a few grains showing a weak core–rim structure (Fig. 5d). Ages of the unzoned grains scatter from 30·5 to 24·1 Ma, with two statistical peaks at 27·1 ± 0·3 Ma (MSWD 1·9, *N* 10/21) and 25·0 ± 0·6 Ma (MSWD 1·8, *N* 6/21). Rim analyses are significantly younger than unzoned grains and scatter from 23·0 to 18·5 Ma; however, there is no difference in trace element composition between the grains (SD Electronic Appendix Fig. 5f). Sample N12 may contain excess ^{206}Pb and the weighted average Th–Pb age of unzoned grains is reported (24·4 ± 0·3 Ma, MSWD 1·3, *N* 16/21). Polymineralic inclusions of K-feldspar and quartz were observed in the unzoned grains.

Monazite grains in metapsammite N10 commonly have concentric zoning with large BSE-dark cores and narrow BSE-grey rims (Fig. 5e). Cores yield older ages with a tight average age of 29·5 ± 0·3 Ma (MSWD 1·5, *N* 15/15). The unzoned or rim analyses scatter from 27·4 to 20·6 Ma. K-feldspar and quartz polymineralic inclusions were observed in the monazite cores. Cores have relatively higher HREE and Y contents than the four rim analyses (including unzoned) (Figs 6d and 7c). All of the analyses show strong Eu anomalies (Eu/Eu* 0·09–0·15).

GARNET TRACE ELEMENT COMPOSITION

Garnet is present in several of the investigated samples (Table 1) where it is a major phase rich in HREE and Y. Its growth probably affected the trace element composition of monazite. Trace element traverses were analyzed for garnet porphyroblasts and small garnet grains from samples NL01, NL27 and N10. Major element traverses or maps of garnet in the same thin sections were previously published by Wang *et al.* (2013). The Fe, Mg, Mn and Ca compositions of garnet porphyroblasts in all three samples were homogenized by high-temperature cation diffusion and exhibit similar flat zoning patterns. At the outmost rims (<100 μm), Mn and Fe/(Fe + Mn) increase and Mg decreases. This is attributed to back-diffusion of Mn and exchange of Fe and Mg with biotite (Kohn *et al.*, 2004).

Table 2: Summary of monazite and rutile U–Pb ages, and monazite and garnet trace element signatures

Sample	Locality	Monazite inclusions	Monazite age (Ma)	Monazite REE	Rutile age (Ma)
NL01	Lower GHC, Nyalam	None	Cores 18·6 ± 0·6 Ma, rims 16·1–15·4 Ma, rims 14·1 ± 0·4 Ma	Core to rim, increase in HREE and Y	
L11	Lower GHC, Langtang	Pl + Bt + Ms + Qz (core + mantle)	Cores 26·0 ± 0·6 Ma, mantles 24·1–18·7 Ma, rims 17·8–14·2 Ma	Cores to mantle, decrease in HREE and Y Mantle to rim, increase in HREE and Y	6·9 ± 0·3
N24	Lower GHC, Nyalam	Ab + Or + Qz (rim), Grt + Ms + Bt (core)	Cores + rims 17·3 ± 0·2 Ma	Core to rim, increase in HREE	
N22	Lower GHC, Nyalam	Ms + Qz (rim)	Inherited cores 961 ± 13 Ma, overgrowth rims 15·3 ± 0·2 Ma	Core to rim, increase in HREE and Y	
N18	Lower GHC, Nyalam	Abundant Sil, Kfs + Qz + Grt + Ms + Bt + Pl	Cores + rims 18·2 ± 0·2 Ma (excess ^{206}Pb, Th–Pb age ~ 16·7 Ma)	No difference in HREE and Y	
NL27	Upper GHC, Nyalam	(Kfs + Pl + Qz) polymineralic inclusion (mantle)	Inherited cores 492–463 Ma, mantles 32·0 ± 0·8 Ma, mantles 29·6–27·3 Ma, rims 25·4–20·7 Ma	Core to rim, decrease in HREE	
NL29	Upper GHC, Nyalam	Kfs + Ms + Qz + Sil + Bt + Pl	25·9 ± 0·3 Ma	No difference in HREE and Y (Grt-free sample)	
NY11	Upper GHC, Nyalam	(Kfs + Ms + Qz) polymineralic inclusion + Bt + Pl (core + rim)	Cores 29·2 ± 0·4 Ma, rims 28·4 ± 0·3 Ma	Homogeneous in HREE and Y (Grt-free sample)	16·4 ± 0·4
N12	Upper GHC, Nyalam	(Kfs + Qz) polymineralic inclusion (unzoned)	Unzoned 30·5–29·7 Ma, 27·1 ± 0·3 Ma, 25·0 ± 0·6 Ma, rims 23·0–18·5 Ma (excess ^{206}Pb, Th–Pb age 24·4 ± 0·3 Ma)	No difference in HREE and Y (Grt-free sample)	15·7 ± 0·2
N10	Upper GHC, Nyalam	(Kfs + Qz) polymineralic inclusion + Bt + Pl (core)	Cores 29·5 ± 0·3 Ma, rims 27·4–20·6 Ma	Cores to rims, decrease in HREE and Y	

Despite the lack of zoning in major elements, garnet preserves significant variations in trace element composition, particularly in HREE and Y (SD Electronic Appendix Fig. 6), owing to their much slower diffusion rates than major elements (Lanzirotti, 1995; Hermann & Rubatto, 2003). Large garnet porphyroblasts commonly have high HREE contents in the cores and show distinct decreases toward the rims, with a transitional mantle zone in some samples (NL01 and N10). Y contents in garnet do not always correlate with HREE contents and are less diagnostic in defining internal zoning. In the mantle of the NL01 garnet, Y increases and has an opposite trend to the HREE. The compositions of small garnet grains vary in each sample. In sample NL01 the HREE and Y contents of small garnets are higher than those of the porphyroblast cores; in samples N10 and NL27, they are similar to the compositions of the porphyroblast rims. Chondrite-normalized REE patterns of garnet in all the samples show light REE (LREE) depletion below chondrite values, negative Eu anomalies and relative HREE enrichment (Fig. 8). The negative Eu anomalies and LREE depletion are similar across different garnet domains, whereas the HREE enrichment is always a maximum in the cores of large garnet porphyroblasts. From cores to rims, HREE enrichment gradually decreases and rims show relatively flat HREE patterns or slight depletion compared with the middle REE (MREE).

RUTILE U–Pb GEOCHRONOLOGY AND THERMOMETRY

Most rutile grains are clear, have euhedral crystal shapes and vary in color from brown to dark yellow. Grain sizes vary from ~60 to >150 μm in radius (brachyaxis) and are relatively larger in samples L11 and N12. Most rutile grains are homogeneous and do not show any internal zoning in BSE images (Fig. 9). Analyses that have unusually high concentrations of Si, Zr, Hf, Y, Fe, Mn or Th were discarded owing to possible contamination by inclusions such as zircon, monazite and ilmenite.

Rutile crystals from samples L11, NY11 and N12 have relatively high concentrations of U (mostly > 40 ppm; SD Electronic Appendix Table 5) and were analyzed for U–Pb dating. Rutile crystals in metapelite sample L11 yield ages that scatter between 8·7 and 4·4 Ma (Fig. 9) with a significant peak at 6·9 ± 0·3 Ma (MSWD 1·2, *N* 8/13). Rutile crystals in metapsammite sample NY11 yield ages that define a peak at 16·4 ± 0·5 Ma (MSWD 1·5, *N* 12/15). Rutile crystals in metapsammite sample N12 have higher U concentrations of 300–400 ppm and a low fraction of common Pb (most < 0·5%). Ages for this sample tightly cluster at 15·7 ± 0·2 Ma (MSWD 1·1, *N* 31/31).

Rutile crystals from samples NL01, L11, NL07 (adjacent to N24), NL16 (adjacent to N22), NY11 and N12 were analyzed for their Zr content; average temperatures and uncertainties are reported in Table 1. Samples

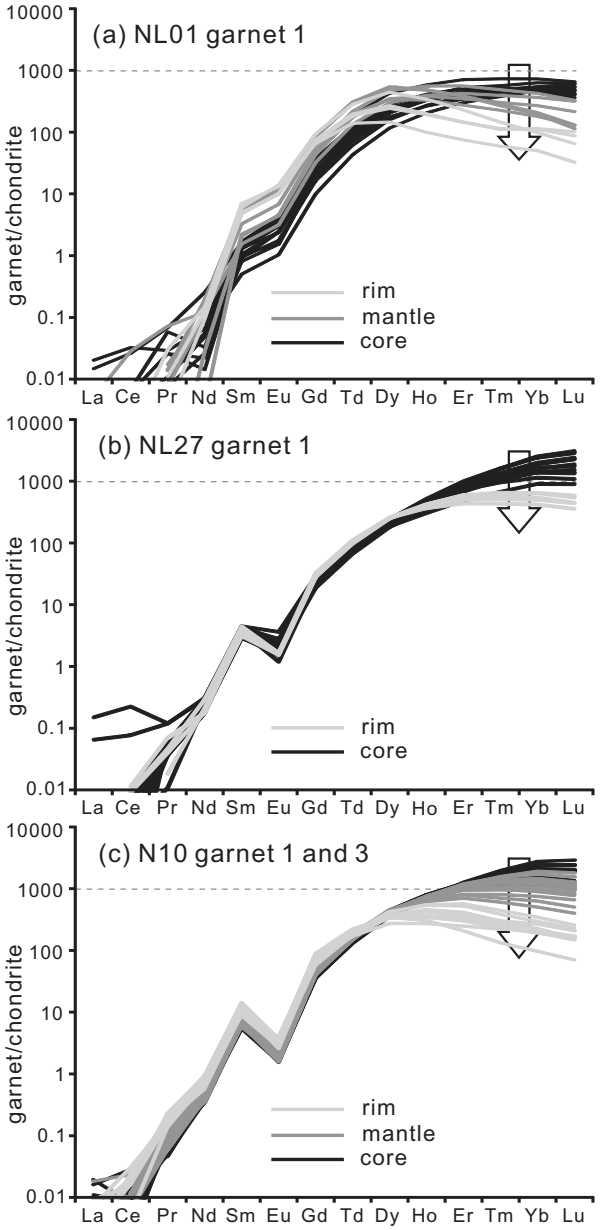

Fig. 8. Chondrite-normalized REE patterns of garnet. The arrows highlight changes in HREE between different growth zones.

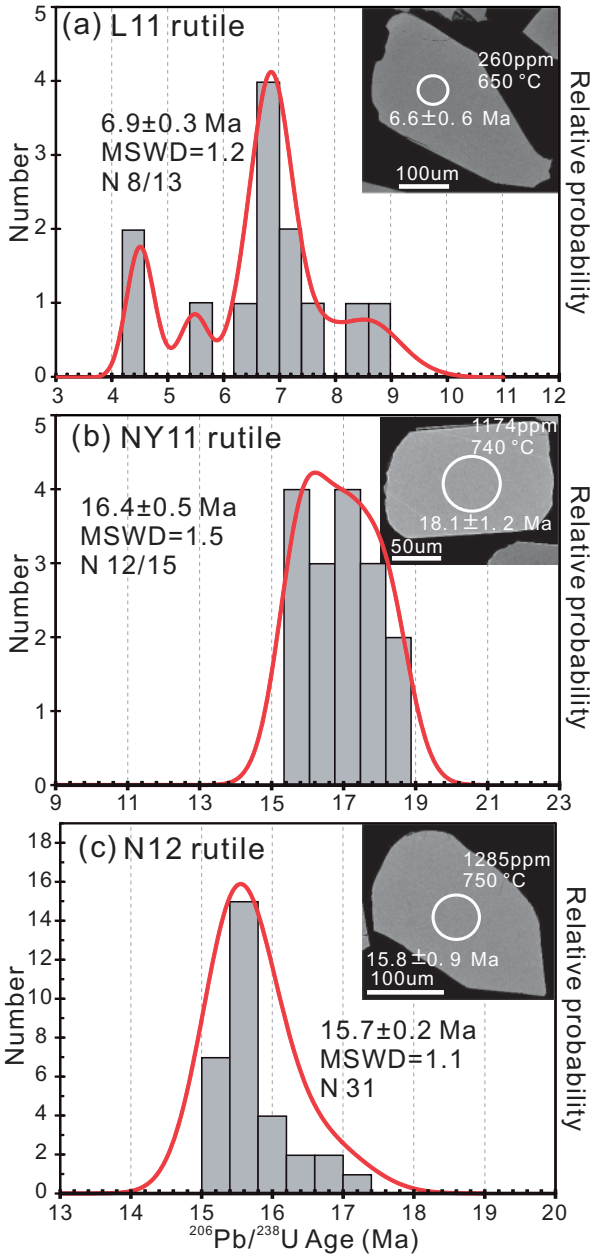

Fig. 9. Representative back-scattered electron images of selected rutile crystals and probability diagrams with superimposed histograms of rutile U–Pb ages. Circles indicate the location of the LA-ICP-MS analyses and are ~62 μm in diameter. Numbers indicate $^{206}Pb/^{238}U$ ages, Zr concentrations and calculated temperatures using the Zr-in-rutile thermometer of Tomkins *et al.* (2007).

NL01 and L11 from the kyanite zone have the lowest Zr contents of ~200–380 ppm, which yield average temperatures of 640 ± 35°C and 660 ± 35°C, respectively. Samples NL07 and NL16 from the sillimanite–muscovite zone have slightly higher Zr contents of ~250–500 ppm and ~350–700 ppm, respectively. Calculated average temperatures are 655 ± 35°C and 675 ± 35°C, respectively. Samples NY11 and N12 from the upper GHC have significantly higher Zr contents (~1000–1400 ppm), which yield average temperatures of 730 ± 40°C and 745 ± 40°C, respectively. In summary, the upper GHC samples have a tendency to record 50–100°C higher temperatures than the lower GHC samples, although the uncertainties are relatively large.

DISCUSSION

Linking monazite ages to metamorphic conditions

Accurate interpretation of the ages obtained from accessory phases is challenging as they can grow at different stages of the *P–T* path. In this study, the following criteria are used to define the timing of monazite formation with respect to other minerals and rock evolution.

1. Inclusions in monazite are taken as a reflection of the mineral assemblage in which the monazite grew.
2. Monazite HREE and Y signatures can indicate the relative timing of monazite, xenotime and garnet growth. Xenotime was not observed in thin sections and garnet is considered to have a major control on the HREE budget in these samples. In a closed system, garnet growth will consume HREE and Y from the environment and thus reduce their distribution in monazite (Foster *et al.*, 2002; Hermann & Rubatto, 2003; Buick *et al.*, 2006; Rubatto *et al.*, 2006). In contrast, garnet breakdown will release HREE and Y, which can then be redistributed in monazite growing at the same time.
3. Negative Eu anomalies in monazite REE patterns are an indicator of feldspar modal abundance. Among the feldspars, K-feldspar has a stronger positive Eu anomaly than plagioclase and is efficiently produced during muscovite and biotite melting, whereas plagioclase is consumed during prograde melting (Groppo *et al.*, 2012). Therefore, the accumulated negative Eu anomaly in monazite may reflect the progression of melting (Rubatto *et al.*, 2006, 2013).

In this study, inclusions of sillimanite, K-feldspar, muscovite, biotite, plagioclase and quartz (+ garnet in sample N18; see summary in Table 2) are present in monazite from two samples located on opposite sides of the Nyalam Discontinuity (N18 and NL29). In the studied samples this mineral assemblage is stable only in the sillimanite–K-feldspar stability field, close to peak temperature conditions. Most monazite grains in sample NL29 have euhedral shapes and faint oscillatory zoning, suggesting that they may have crystallized from a melt (Rubatto *et al.*, 2013). Notably, monazite in each of these samples yields a single age cluster (18·2–16·7 Ma and 25·9 ± 0·3 Ma) and is also homogeneous in HREE and Y. These results are taken to indicate that monazite in samples N18 and NL29 crystallized from a melt close to peak temperature conditions.

In monazite from the lower GHC sample NL01, HREE and Y contents increase from core to rim (Figs 6a and 7a). Pseudosection modeling from Wang *et al.* (2015) shows that for the lower GHC metapelitic samples in the Nyalam transect, garnet modal abundance increases during burial and is reduced during decompression and cooling. Therefore, the HREE- and Y-enriched monazite rims in sample NL01 (16·1–15·4 Ma and 14·1 ± 0·4 Ma) are interpreted to grow during decompression associated with garnet breakdown, a process that has been commonly observed in kyanite-grade samples from the Nyalam transect (Wang *et al.*, 2015). The HREE- and Y-depleted core ages of sample NL01 (18·6 ± 0·6 Ma) are interpreted as dating prograde conditions associated with garnet growth. Because the ages of the cores yield a single cluster and are very close to the rim ages, it is more likely that they (re)crystallized at kyanite grade, close to peak pressure conditions (Wang *et al.*, 2015). For the sillimanite–muscovite-grade sample N24, the polymineralic inclusions of albite and orthoclase observed in monazite rims represent crystallized melt (Icenhower & London, 1995; Cesare *et al.*, 2009). Melt in this sample probably formed through H_2O-saturated melting because prograde muscovite is still present (Wang *et al.*, 2015). This observation supports our interpretation that the monazite rims in sample N24 (17·3 ± 0·2 Ma) yield an age after H_2O-saturated melting.

Monazites in the upper GHC samples (NL27, NY11, N12 and N10) contain polymineralic inclusions of K-feldspar + quartz. Similar inclusions with negative crystal shapes are abundant in garnet and are interpreted as 'nanogranites' that represent crystallized melt (Cesare *et al.*, 2009; Ferrero *et al.*, 2012; Groppo *et al.*, 2012). For the sillimanite-grade upper GHC samples, the observed polymineralic inclusions are also consistent with the mineral assemblage at peak temperature conditions, which was produced through muscovite dehydration melting (Imayama *et al.*, 2010; Groppo *et al.*, 2012; Wang *et al.*, 2013). Stronger negative Eu anomalies in these monazites compared with those formed in K-feldspar-absent samples (NL01 and L11) also suggest that these GHC monazite domains grew in the presence of K-feldspar. Therefore, we interpret that at least part of the monazite (re)crystallized during anatexis and ages from these samples (NL27 32 ± 0·8 Ma and 29·6–27·3 Ma, NY11 28·6 ± 0·3 Ma, N12 27·1–24·5 Ma and N10 29·5 ± 0·3 Ma) are interpreted to date formation after muscovite dehydration melting. In samples NL27 and N10, monazite HREE or Y contents decrease from older domains (NL27 32 ± 0·8 Ma and 29·6–27·3 Ma, N10 29·5 ± 0·3 Ma) to younger domains (NL27 25·4–20·7 Ma, N10 27·4–20·6 Ma, Figs 6 and 7). The same core–rim decrease in HREE is observed in the garnet porphyroblasts of samples NL27 and N10. This indicates that these age intervals are associated with garnet growth. For the sillimanite-grade upper GHC samples, garnet modal abundance could increase during burial to P_{max}. Another possibility for garnet growth is along a heating and decompression path from P_{max} to T_{max} (Harris *et al.*, 2004; Groppo *et al.*, 2009, 2012; Zhang *et al.*, 2015) through the sliding reaction Als + Bt + Pl + Qz = Grt + Kfs + melt, which did occur in sample N10. Because mineral inclusions observed in the older monazites indicate that these samples have already been through muscovite dehydration melting at ~32–25 Ma, the low-HREE rims (25–20 Ma) are thus interpreted as dating the timing from P_{max} to T_{max} associated with peritectic garnet growth.

Sample L11 from the lower GHC section in Langtang contains monazites that have three concentric growth domains with decreasing age outward. Specifically, HREE and Y contents decrease from core to mantle, suggesting that the monazite cores and mantles grew during prograde metamorphism associated with garnet growth. Previous studies in Barrovian metapelites have shown that metamorphic monazite starts to grow at

garnet grade (Pyle *et al.*, 2001; Wing *et al.*, 2003; Spear & Pyle, 2010) or staurolite grade (Kohn & Malloy, 2004) through breakdown of REE-rich minerals such as allanite (Janots *et al.*, 2007). Therefore, the core age (26·0 ± 0·6 Ma) probably records the first growth of monazite at prograde garnet or staurolite grade when HREE and Y were still abundant in the reactive bulk. Monazite mantle ages scatter between ~24·1 and 18·7 Ma and are interpreted to record growth from garnet or staurolite grade to peak conditions. Rim compositions show an inverted chemical trend with increasing HREE and Y, suggesting that monazite rims (17·8–14·2 Ma) grew during decompression associated with garnet breakdown.

The discussion above has shown that the monazite cores in samples NL01 and N10 and mantles in sample NL27 formed at prograde near-peak conditions (Table 2). This allows us to calculate partition coefficients for REE between monazite and garnet ($^{REE}D_{Mnz/Grt}$) at amphibolite-facies conditions, using the average trace element compositions of mineral domains (SD Electronic Appendix Table 6). The $^{REE}D_{Mnz/Grt}$ values for amphibolite-facies conditions show a similar trend to that defined by granulite-facies rocks metamorphosed at ~800°C (SD Electronic Appendix Fig. 8; Hermann & Rubatto, 2003; Buick *et al.*, 2006; Rubatto *et al.*, 2006); $^{MREE}D_{Mnz/Grt}$ values are consistent and largely overlapping with those defined by Hermann & Rubatto (2003) and Rubatto *et al.* (2006), but lower than the Buick *et al.* (2006) results; $^{HREE}D_{Mnz/Grt}$ values show a larger spread that is, however, within the range of values reported for granulite-facies rocks. Specifically, $^{Y}D_{Mnz/Grt}$ values range from 23 to 47 whereas $^{Yb}D_{Mnz/Grt}$ values range from 3·3 to 8·2, indicating that the HREE are preferentially partitioned into monazite relative to garnet.

Many studies have reported inherited ages in Himalayan monazites (e.g. Harrison *et al.*, 1995; Martin *et al.*, 2007; Imayama & Suzuki, 2013; Lederer *et al.*, 2013) and two samples in this study also exhibit apparent inherited ages. The ~961 Ma monazite core in sample N22 probably dates the crystallization age of the protolith granite. Similar ages from detrital zircons of the GHC have been interpreted as relating to magmatism in the East African part of the Pan-African orogeny (e.g. DeCelles *et al.*, 2000). The Paleozoic ages of 463–492 Ma for the monazite of sample NL27 are more common in Himalayan samples and have been related to an early Palaeozoic orogenesis along the Indian margin of Gondwana (e.g. Cawood *et al.*, 2007).

Rutile: peak Zr-temperatures and cooling U–Pb ages

Zr-temperatures and U–Pb ages in rutile are expected to be decoupled in samples that experienced relatively high temperatures because Zr and Pb have different diffusion rates in rutile. According to Zr-diffusion experiments (Cherniak, *et al.*, 2007), 100 μm radius rutile grains require temperatures of <680–710°C to maintain Zr signatures in their cores if cooling fast at rates of 10–30°C Ma^{-1}, comparable with those proposed for the GHC (Imayama *et al.*, 2012; Sorcar *et al.*, 2014). However, studies of natural samples indicate that Zr-in-rutile has a lower diffusion rate than that which can be inferred from experiments and that it is robust even to temperatures of ≥900°C (Jiao *et al.*, 2011; Kooijman *et al.*, 2012; Ewing *et al.*, 2013). In this study, the rutile grains used for trace element analyses have radii of 50–200 μm. Temperatures calculated using Zr-in-rutile thermometers are 640–680°C in the lower GHC and 730–750°C in the upper GHC (Table 2). These results are consistent with published temperature results using the garnet–biotite Fe–Mg thermometer (Wang *et al.*, 2013; Table 1). Rutile is indeed the Ti-rich phase that is predicted to be stable in these assemblages at peak conditions (Imayama *et al.*, 2010, 2012; Wang *et al.*, 2013, 2015). We thus conclude that in these GHC samples, Zr diffusion is insignificant and that the Zr-in-rutile thermometer is robust up to upper-amphibolite-facies temperatures (~750°C).

For the rutile U–Pb ages, it is more likely that these ages record the timing when the sample cooled below the Pb diffusion closure temperatures rather than the timing of rutile growth, for the following reasons: (1) the metamorphic temperatures of the GHC rocks (640–750°C, Wang *et al.*, 2013) are higher than the Pb-in-rutile diffusion closure temperatures (550–630°C, Cherniak, 2000; Kooijman *et al.*, 2010; Zack *et al.*, 2011) and thus the U–Pb system was probably reset during the temperature peak; (2) rutile U–Pb ages are significantly younger than monazite ages that represent near-peak or cooling ages. Closure temperature of U–Pb in accessory minerals mainly depends on grain radius and cooling rate, with larger crystals that cooled faster having higher closure temperatures (Cherniak, 2000; Cherniak *et al.*, 2004). Volume diffusion experiments for Pb show that rutile has a closure temperature of 567–617°C for 70–200 μm radius grains (cooling rate 1°C Ma^{-1}; Cherniak, 2000). Recent studies of Pb diffusion in natural rutile samples show a more complex picture and give closure temperatures varying from 569 ± 24°C (60–135 μm radius, cooling rate 1–2°C Ma^{-1}, Kooijman *et al.*, 2010) to 630°C (50–100 μm radius, cooling rate 3°C Ma^{-1}, Vry & Baker, 2006). Considering that most rutile grains in samples L11, NY11 and N12 have radii of 50–200 μm and that the GHC underwent rapid cooling (average cooling rate >10–30°C Ma^{-1}, Imayama *et al.*, 2012; Sorcar *et al.*, 2014), a conservative temperature of 560–620°C is used as the Pb-in-rutile closure temperature.

Rutile U–Pb age data yield a tight cluster for sample N12, but show different degrees of scatter in samples NY11 and L11 (Fig. 9). Two factors may contribute to the scatter of ages in these samples: (1) rutile has low U concentrations and for such young Himalayan samples detection of the radioactive ^{206}Pb yields relatively large uncertainties (up to 9%); (2) the samples cooled slowly across the Pb-in-rutile closure temperature and thus

recorded a range of ages. Therefore, only statistically consistent age clusters were reported ($N > 5$). The obtained rutile ages (L11 6·9 ± 0·3 Ma, NY11 16·4 ± 0·5 Ma, N12 15·7 ± 0·2 Ma) are 10–12 Myr younger than the near-peak metamorphic ages revealed from monazite, and give information on the duration of cooling from near-peak temperature conditions to 560–620°C.

Timing of partial melting and cooling history

In the age summary of Fig. 10a there is a marked difference in monazite and rutile ages from lower GHC samples (monazite age populations between 26 and 14 Ma, rutile ages ~7 Ma) to upper GHC samples (monazite age populations between 32 and 20 Ma, rutile ages ~16–17 Ma), indicating different times of metamorphism for the two blocks. Together with the petrology and *P–T* conditions of these samples (Wang *et al.*, 2013), these data are used to reconstruct the timing of partial melting in the two blocks (Fig. 10b). In addition, cooling histories are defined using the monazite and rutile ages from this study and published mineral cooling ages from the Nyalam transect. The additional cooling ages used are muscovite $^{40}Ar/^{39}Ar$ ages (Wang *et al.*, 2006) with a closure temperature of 400 ± 50°C (Hames & Bowring, 1994), zircon fission-track ages (Wang *et al.*, 2010) with closure temperature of 280 ± 20°C (Tagami *et al.*, 1998) and apatite fission-track ages (Zheng *et al.*, 2014) with a closure temperature of 100 ± 10°C (Gleadow & Duddy, 1981).

Lower GHC block

At ~26 Ma, monazite began to form at sub-solidus prograde conditions (garnet or staurolite grade, 500–600°C). Monazites that grew at this stage have relatively high HREE and Y contents (cores of L11). From 26 to 19 Ma the lower GHC block underwent prograde metamorphism towards peak conditions. Monazite grew in equilibrium with garnet and recorded decreasing HREE and Y contents (mantles of L11). At 19–16 Ma, most samples reached peak metamorphic conditions (640–675°C) and most monazites grew at this stage (cores of NL01, N24 and N18). After the metamorphic peak, the lower GHC samples underwent different degree of decompression from the peak pressures (10–13 kbar) to ~4 kbar (Wang *et al.*, 2013, 2015) and newly forming monazite had higher HREE and Y contents owing to garnet breakdown (rims of NL01, L11, N22). The degree of partial melting that the metapelitic rocks experienced varies and largely depends on the pressures reached by the samples. Partial melting in most metapelitic samples (NL01, L11 and N24) was limited to a few per cent (~5–7%) and was the result of an H_2O-saturated melting reaction (Table 1). During decompression, when the sample entered the muscovite-dehydration field (4 kbar, N18) a larger percentage of melt was produced (~20 ± 5%). Initial cooling probably began at ~16 Ma. From ~16 to 7 Ma, the lower GHC block cooled slowly from peak temperatures to rutile U–Pb closure

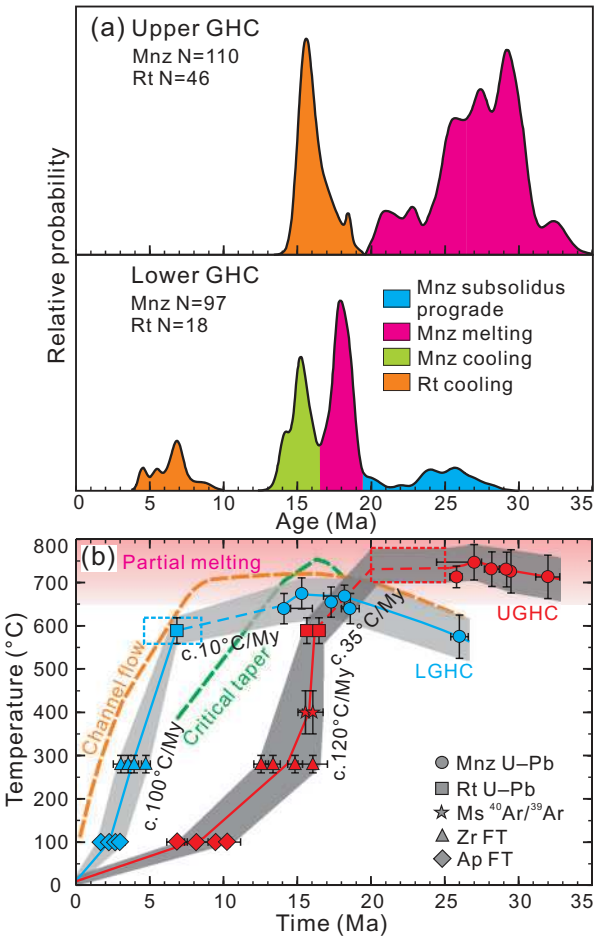

Fig. 10. Summary of monazite and rutile age trends of the upper and lower GHC blocks; data from this study. (a) Probability diagrams of monazite and rutile ages that are linked to different metamorphic stages. (b) Temperature–time histories of the upper and lower GHC blocks and predictions from channel flow and critical taper models. Filled squares or circles are statistically consistent average ages. Dashed red rectangle is the age interval defined by monazite rims from samples NL27 and N10. Dashed blue rectangle is the age interval from rutile sample L11. Black bars illustrate the uncertainties in calculated temperatures or ages. Monazite (re)crystallization temperatures are from Zr-in-rutile results in this study or the thermobarometric results of Wang *et al.* (2013). Temperatures for other minerals are diffusion closure temperatures (see text for details). Muscovite $^{40}Ar/^{39}Ar$ ages and zircon and apatite fission-track (FT) ages are from the literature (Wang *et al.*, 2006; Wang *et al.*, 2010; Zheng *et al.*, 2014). LGHC, lower GHC; UGHC, upper GHC.

temperatures (560–620°C) with an average cooling rate of ~10 ± 5°C Ma^{-1}. From ~7 Ma, this block underwent much faster cooling to zircon or apatite fission-track closure temperatures with an average cooling rate of 100 ± 20°C Ma^{-1}.

Upper GHC block

No monazite that grew in sub-solidus prograde conditions was preserved. The oldest preserved monazites (mantles of NL27) grew at ~32 Ma, during prograde anatexis after muscovite dehydration melting and incorporated relatively high HREE contents. For Himalayan

sillimanite-grade metapelites, the temperature conditions of the muscovite dehydration melting reaction have been constrained to be 650–750°C (5–9 kbar) for a variety of compositions (e.g. Groppo *et al.*, 2010, 2012; Imayama *et al.*, 2012; Sorcar *et al.*, 2014). From ~30 to 25 Ma most samples reached the sillimanite–K-feldspar stability field close to peak temperature conditions (730–750°C) and abundant melt was produced through muscovite dehydration melting. Most monazites (re)crystallized at this stage and show a strong negative Eu anomaly (NL27, NY11 and N10) and moderate HREE contents (mantles of NL27). Anatexis during heating and decompression probably lasted until 25–20 Ma, as recorded by the monazite rims in samples NL27 and N10, which have the lowest HREE and Y contents and were associated with peritectic garnet growth. From ~20 to 16 Ma the upper GHC block gradually cooled from peak temperatures to rutile U–Pb closure temperatures (560–620°C) with an average cooling rate of ~35 ± 8°C Ma^{-1} (Fig. 11b). After ~16 Ma this block underwent a much faster cooling to zircon fission-track closure temperatures with an average cooling rate of 120 ± 40°C Ma^{-1}.

Our results indicate that blocks within the GHC underwent at least two stages of cooling at different rates (Fig. 11b), rather than monotonous cooling. A period of relatively slow cooling from peak *T* to 560–620°C was followed by rapid cooling to ~280°C. During this evolution, each block of the GHC resided at relatively high temperatures (>600°C) for a relatively long period of ~15 Myr. The duration of partial melting at near-peak conditions lasted for ~3 Myr in the lower GHC and as long as 7–12 Myr in the upper GHC. Long residence at high temperatures has been reported for other regions of the Himalaya such as the Leo Pargil dome of northwestern India (Lederer *et al.*, 2013), the Annapurna region of central Nepal (Kohn & Corrie, 2011), east–central Nepal (Larson *et al.*, 2011, 2013), the Mount Everest region (Cottle *et al.*, 2009), eastern Nepal (Imayama *et al.*, 2012) and Sikkim (Rubatto *et al.*, 2013), and might be a common feature across the orogenic belt.

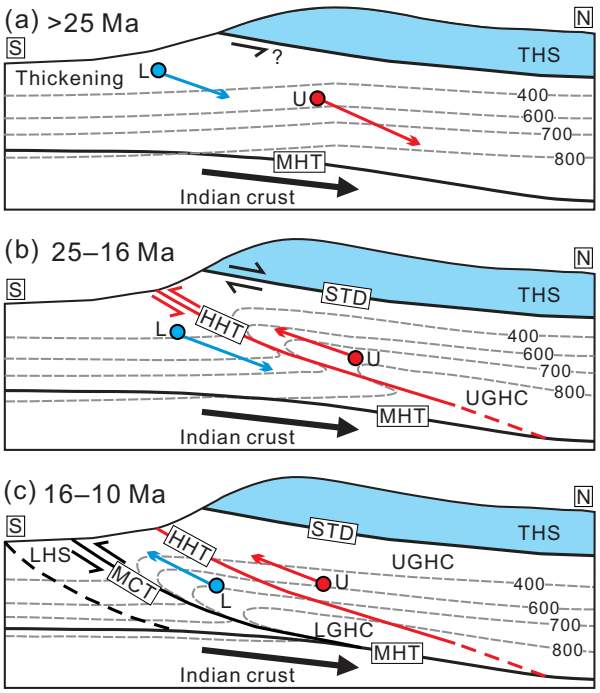

Fig. 11. Simplified tectonic scenario illustrating in-sequence thrusting during the exhumation of the GHC in the central Himalaya (see text for details). L and U indicate particles in the lower and upper GHC, respectively. Dashed gray lines with numbers are temperature isograds. HHT, High Himalayan Thrust; MHT, Main Himalayan Thrust.

Discontinuities within the GHC and overview

The established timescale for the GHC in the Nyalam region indicates that the upper GHC block underwent partial melting and cooling ~5–10 Myr earlier than the lower GHC block (Fig. 10). In addition, upper GHC rocks also yield ~60–80°C higher peak temperature conditions and reached a higher degree of melting than the lower GHC rocks. These results point to a discontinuity within the GHC in the Nyalam region. The position of the discontinuity inferred from the geochronological and petrological data is consistent with the location of the Nyalam Discontinuity recognized previously by a *P–T* inversion of ~40°C and ~3 kbar toward higher structural levels (Wang *et al.*, 2013). Although most metapelites from the upper GHC reached their temperature peak at relatively low pressures (Wang *et al.*, 2013), plagioclase–amphibole gneisses from this section record metamorphic pressure of 10·6 ± 1·2 kbar (Zhang *et al.*, 2012), indicating that the upper GHC rocks were once buried to ~30–40 km depth and were juxtaposed with the lower GHC at a later time. Kinematically, this discontinuity is marked by slightly mylonitized paragneisses and augen orthogneisses with top-to-the-south shear sense (Wang *et al.*, 2013). However, it is difficult to determine the width of this shear zone owing to pervasive deformation across the GHC (Larson, 2012; From & Larson, 2014). Extensive high-temperature recrystallization throughout the GHC (Reddy *et al.*, 1993; Larson & Cottle, 2014) would also hinder the development of mylonitic structures. We argue that a metamorphic and geochronological discontinuity lies between the upper and lower GHC of the Nyalam region, and separates the GHC into two portions. The upper GHC was buried earlier than the lower GHC to higher temperatures and to a possibly similar depth, and was then thrust on top of the lower GHC along the Nyalam Discontinuity.

In the adjacent Langtang region, discontinuities within the GHC were first proposed based on detailed fabric analyses (Reddy *et al.*, 1993) and high-precision thermobarometric data (Fraser *et al.*, 2000). The Langtang Thrust was subsequently identified based on geochronological and thermobarometric data (Kohn *et al.*, 2004; Kohn, 2008). This thrust is located at a

similar position to the Nyalam Discontinuity and is close to the K-feldspar-in isograd. Initial cooling of the lower GHC in Langtang is constrained to be at ~16 Ma (Kohn *et al.*, 2004), consistent with what we report for the Nyalam region. Initial cooling of the upper GHC in Langtang is constrained at around 21 Ma. Metamorphic conditions in both regions are similar, with rocks in the hanging wall yielding ~50–70°C higher temperatures than the footwall rocks (Kohn, 2008). Because these two adjacent regions are so close (<50 km) and have similar metamorphic conditions and timing, we argue that the Nyalam Discontinuity and Langtang Thrust are connected and that blocks in these two regions underwent the same evolution.

Discontinuities within the GHC have also been reported in other regions along the strike of the Himalayan orogenic belt. In the Lower Dolpo region of western Nepal a high-temperature top-to-the-SW shear zone has been recognized (Fig. 1a, Toijem shear zone; Carosi *et al.*, 2007). This shear zone was active between ~26 and 17 Ma, as constrained by U–Pb dating of monazite in a mylonitic mica-schist and cross-cutting leucogranite dyke (Carosi *et al.*, 2010). Some 100 km to the west, another 4 km thick shear zone (Mangri shear zone) has been recognized and its activity dated at ~25–18 Ma (Montomoli *et al.*, 2013). In central–western Nepal, two discontinuities have been identified (Martin *et al.*, 2010; Corrie & Kohn, 2011) and the initial activation of the structurally higher Sinuwa Thrust (<25 Ma, Corrie & Kohn, 2011) is close in timing to the Nyalam Discontinuity. In east–central Nepal a discontinuity in the temperatures of deformation has been recognized within the GHC (Larson & Cottle, 2014), but may lie below the Nyalam Discontinuity because all the samples of Larson & Cottle (2014) were collected from lower in the GHC compared with samples collected in this study. The timing of metamorphism across this discontinuity is indistinguishable and dated to be from ~24 to 16 Ma (Larson & Cottle, 2014; From *et al.*, 2014), which corresponds to the prograde metamorphism of the lower GHC from this study. In eastern Nepal, the High Himal Thrust (HHT) was recognized by Goscombe *et al.* (2006), based on the finding of a 100–400 m thick shear zone, but no jump in *P–T* conditions has been documented (Imayama *et al.*, 2012). The timing of initial cooling was established to be 27–23 Ma in the hanging wall and 18–16 Ma in the footwall (Imayama *et al.*, 2012), and is similar to that for the Nyalam region. Further to the east in Sikkim, a discontinuity within the GHC was recognized on the basis of monazite and zircon U–Pb ages (Rubatto *et al.*, 2013). However, this discontinuity differs from those recognized in Nepal in that the timing of prograde melting and peak conditions is older in the footwall (~31–27 Ma) and younger in the hanging-wall section (~26–23 Ma; Rubatto *et al.*, 2013). Monazite U–Th–Pb dating of the lowest GHC in this section constrains the timing of partial melting to be ~23–19·5 Ma (Mottram *et al.*, 2014), which allows for the identification of a new discontinuity between the lowest GHC and the ~31–27 Ma sequence of Rubatto *et al.* (2013). In Bhutan, the discontinuity within the GHC is termed the Kakhtang Thrust, which separates a hanging wall that records younger metamorphic ages (14–13 Ma) from a footwall that exhibits older metamorphic ages (21–17 Ma) (Hollister & Grujic, 2006; Grujic *et al.*, 2011; Warren *et al.*, 2011). This thrust is thus considered as an out-of-sequence thrust.

This overview clarifies the presence of an in-sequence thrust within the GHC in the central Himalaya, which extends from western Nepal to central and eastern Nepal and possibly to the Sikkim region, and is locally named the Mangri Shear Zone, Toijem Shear Zone, Sinuwa Thrust, Langtang Thrust, Nyalam Discontinuity and the High Himal Thrust from west to east. According to the present data, this thrust cannot be extended to Bhutan, where an out-of-sequence thrust has been identified. A conservative estimate of length of the thrust is ~800 km oriented parallel to the strike of the Himalayan orogen. This thrust has been named the 'High Himalayan Discontinuity' in west Nepal (Montomoli *et al.*, 2013) and the 'High Himal Thrust' in east Nepal (Goscombe *et al.*, 2006); here we suggest the unifying name 'High Himalayan Thrust'. Further work is needed to investigate whether this thrust is connected to the Main Himalayan Thrust at mid- to deep crustal levels (Fig. 11).

Implications for Himalayan tectonics

The diachroneity of two distinct blocks within the GHC, as well as the different cooling rates within each block, has important implications for tectonic models that have been proposed for the Himalaya. The original channel flow model (HT-1, Jamieson *et al.*, 2004) and other extrusion models such as wedge extrusion (Grujic *et al.*, 1996) and tectonic wedging (Webb *et al.*, 2011) consider the GHC as a coherent segment and assume that the GHC was exhumed by coeval movement along the top-to-south MCT and top-to-north STD. For these models, synchronicity is a necessary factor. However, our results and previous studies (Kohn *et al.*, 2004; Corrie & Kohn, 2011; Grujic *et al.*, 2011; Warren *et al.*, 2011; Imayama *et al.*, 2012; Rubatto *et al.*, 2013) show a diachroneity in the age of peak metamorphism and exhumation across the different portions of the GHC. In Nyalam, the upper GHC block was exhumed ~5–10 Myr earlier than the lower GHC block. This timing implies that movements along the STD and MCT were not simultaneous and that the initial activity of the STD in the Nyalam region (~27–25 Ma, Liu *et al.*, 2012; Xu *et al.*, 2013) was ~10 Myr earlier than that of the MCT (~16 Ma). Therefore, the earlier channel flow models are not compatible with the timescales obtained from this study or other studies of central Himalayan regions. The evolved versions of the channel flow model (HT-111 or HT-111E, Hollister & Grujic, 2006; Jamieson *et al.*, 2006; Jamieson & Beaumont, 2013) are able to incorporate discontinuities and diachronous

metamorphism, where a structurally higher and later dome overlies a structurally lower and earlier GHC sequence. These channel flow models more successfully explain the out-of-sequence pulsed channels observed in Bhutan (Hollister & Grujic, 2006; Grujic *et al.*, 2011; Warren *et al.*, 2011), but are inconsistent with the in-sequence thrusting across the GHC observed in the Nepal Himalaya regions. Another model that considers diachroneity across the GHC is the critical taper model, which suggests exhumation of the GHC by propagating thrusts (Kohn, 2008). The distinct timing of peak metamorphism and cooling across the upper and lower GHC supports the idea that these units were exhumed by in-sequence thrusting along the High Himalayan Thrust and MCT. Such an exhumation model is compatible with the critical taper model.

Another important factor for comparing different tectonic models is the duration of high-temperature metamorphism. The channel flow models highlight the effect of low-viscosity crustal melts, and assume a hot channel that sustained high-temperature conditions for >10–15 Myr (Jamieson *et al.*, 2004, 2006). In contrast, the critical taper model suggests that the duration at high temperatures was only ~5 Myr (Kohn, 2008). In particular, the degree of partial melting in the Nyalam upper GHC was high (15–25%, 730–750°C, muscovite dehydration melting) and sustained for a relatively long duration (7–12 Myr), which favors a low-viscosity middle–lower crust that may have contributed to the exhumation of the upper GHC. On the other hand, partial melting in the lower GHC was not sufficiently high (0–10%, 640–680°C, H_2O-saturated melting) and its duration was shorter (~3 Myr), indicating that melting in the lower GHC rocks exposed at present may not be sufficient to trigger lateral crustal flow. However, protracted high-temperature metamorphism (>600°C for ~15 Myr) in each block suggests that the unexposed deeper rocks have the potential to sustain a longer duration of melting, which may be important for the transport of heat and material in large hot orogens.

In conclusion, the in-sequence thrusting and relatively long duration of high-temperature metamorphism imply that channel flow and critical taper processes are not mutually exclusive (Beaumont & Jamieson, 2010; Larson *et al.*, 2010, 2011; Jamieson & Beaumont, 2013; From *et al.*, 2014; Larson & Cottle, 2014), but evolved spatially and temporally. The channel flow process is more likely to dominate the exhumation of high-grade migmatitic rocks, whereas the critical taper process seems more appropriate for the exhumation of low-grade metamorphic or cooled migmatitic rocks. We propose a simplified scenario to illustrate the tectonic evolution of the GHC in the Nepal Himalaya (Fig. 11). Before ~25 Ma, the upper and lower GHC rocks were progressively buried owing to thickening of the Himalayan orogen. The upper GHC rocks were buried to mid- to lower-crustal levels and reached melting temperatures as early as ~32 Ma, whereas the lower GHC rocks were still at a shallow crustal level. From ~25 to 16 Ma, the upper GHC rocks were exhumed by coeval movement along the STD and High Himalayan Thrust in a setting that was dominated by lateral crustal flow, whereas the lower GHC was continuously buried. From ~16 to ~10 Ma the lower and upper GHC blocks were juxtaposed and exhumed together along the MCT. Because the upper GHC migmatites had already cooled, and the degree and duration of partial melting in the lower GHC was not sufficient to trigger crustal flow, the juxtaposed GHC sequences were exhumed as a critical thrusting wedge. Movements along the High Himalayan Thrust and STD probably ceased at this time. Movement along the MCT ceased at around 10–8 Ma (Harrison *et al.*, 1997; Kohn *et al.*, 2004; Larson *et al.*, 2013) and the thrusting wedge then shifted toward the south to lower structural levels. After ~16 Ma, tunneling channel flow may have still existed, but retreated beneath the edge of the Tibetan plateau (Nelson *et al.*, 1996; Jamieson & Beaumont, 2013) or was exhumed as domes to the north as in the Bhutan region (Hollister & Grujic, 2006; Grujic *et al.*, 2011; Warren *et al.*, 2011).

CONCLUSIONS

Determination of monazite ages in metapelites, metapsammites and orthogneiss indicates that monazite in amphibolite-facies (650–750°C) rocks can record either inherited ages or metamorphic ages at various stages along a Barrovian-type *P–T* path. Accurate interpretation of these ages requires the combined study of monazite zoning, mineral inclusions, age populations, trace element signatures, and bulk-rock *P–T* evolution. Given the complexity and non-continuity of mineral records, dating migmatization requires investigation of several samples from each block. Rutile in amphibolite-facies rocks records cooling ages at its closure temperature. The Zr-in-rutile thermometer is robust at amphibolite-facies conditions and can record peak temperature conditions. Monazite and garnet partition coefficients ($D_{Mnz/Grt}$) from amphibolite-facies samples are consistent with those reported for granulite-facies samples.

The multidisciplinary approaches used in this study allow us to link monazite and rutile U–Pb ages to metamorphic stages and to constrain the timing of partial melting and cooling across the GHC in the Nyalam–Langtang region. The GHC in this region consists of two distinct blocks. The upper GHC block was the first to be buried and reached higher peak temperatures (730–750°C) and a higher degree of partial melting (15–25%), dominated by muscovite dehydration melting. Monazite records the earliest prograde melting at ~32 Ma and large-scale partial melting lasted from 29 to 25 Ma, possibly to ~20 Ma. From ~20 to 16 Ma this block slowly cooled from peak *T* to 560–620°C at an average cooling rate of 35 ± 8°C Ma^{-1}, followed by rapid cooling (120 ± 40°C Ma^{-1}). The lower GHC block experienced lower peak temperatures (640–675°C) and a lower amount of partial melting (0–10%) via H_2O-saturated or muscovite dehydration melting. Monazite

records early sub-solidus prograde ages of ~26 Ma and partial melting lasted from ~19 to 16 Ma, while the upper section was already cooling. From ~16 to 7 Ma, the lower block slowly cooled from peak T to 560–620°C at an average cooling rate of 10 ± 5°C Ma^{-1}, followed by rapid cooling (100 ± 20°C Ma^{-1}). The timescale of metamorphism suggests a long duration (~15 Myr) of high-temperature metamorphism (>600°C). Partial melting in the upper GHC lasted for 7–12 Myr, whereas partial melting in the lower GHC was sustained for only ~3 Myr.

The diachroneity of two distinct blocks within the GHC implies a discontinuity in the study area, which is probably connected to other discontinuities in the central Himalaya. These discontinuities together constitute the High Himalayan Thrust, which was active during the period 25–16 Ma. Diachronous metamorphism and in-sequence thrusting across the GHC is compatible with the critical taper model, whereas a long period at high temperature in each block is more supportive of the channel flow model. For the rocks exposed at present in the Himalaya a channel flow process dominated the exhumation of the high-grade upper GHC during the period 25–16 Ma, whereas a critical taper process dominated the exhumation of the lower GHC rocks and cooled upper GHC migmatites from 16 to 10 Ma. This study implies that both propagating thrusting along large tectonic boundaries and low-viscosity lateral crustal flow contribute to the exhumation of high-grade metamorphic rocks in Himalaya-like large collisional orogens.

ACKNOWLEDGEMENTS

The authors thank P. Holden and J.-W. Park for analytical help with the SHRIMP and LA-ICP-MS. S. M. Rai, M. Wang and X. X. Wang are thanked for help during fieldwork in Himalaya. We greatly appreciate the constructive reviews by T. Imayama and an anonymous reviewer.

FUNDING

This work was supported by the National Natural Science Foundation of China (grant numbers 41172176 and 41121062), China Geological Survey and China Scholarship Council (grant number 201306010046).

SUPPLEMENTARY DATA

Supplementary data for this paper are available at *Journal of Petrology* online.

REFERENCES

Aleinikoff, J. N., Schenck, W. S., Plank, M. O., Srogi, L., Fanning, C. M., Kamo, S. L. & Howell, B. (2006). Deciphering igneous and metamorphic events in high-grade rocks of the Wilmington Complex, Delaware: morphology, cathodoluminescence and backscattered electron zoning, and SHRIMP U–Pb geochronology of zircon and monazite. *Geological Society of America Bulletin* **118**, 39–64.

Andersen, T. (2002). Correction of common lead in U–Pb analyses that do not report ^{204}Pb. *Chemical Geology* **192**, 59–79.

Arita, K. (1983). Origin of the inverted metamorphism of the Lower Himalayas, central Nepal. *Tectonophysics* **95**, 43–60.

Beaumont, C. & Jamieson, R. A. (2010). Himalayan Tibetan orogeny: channel flow versus (critical) wedge models, a false dichotomy. In: Leech, M. L., Klemperer, S. L. & Mooney, W. D. (eds) *Proceedings for the 25th Himalaya–Karakoram–Tibet Workshop. US Geological Survey Open-File Report* **2010**, 1099. [Available at http://pubs.usgs.gov/of/2010/1099/beaumont/.]

Beaumont, C., Jamieson, R. A., Nguyen, M. H. & Lee, B. (2001). Himalayan tectonics explained by extrusion of a low-viscosity crustal channel coupled to focused surface denudation. *Nature* **414**, 738–742.

Bollinger, L., Henry, P. & Avouac, J. P. (2006). Mountain building in the Nepal Himalaya: Thermal and kinematic model. *Earth and Planetary Science Letters* **244**, 58–71.

Buick, I. S., Hermann, J., Williams, I. S., Gibson, R. L. & Rubatto, D. (2006). A SHRIMP U–Pb and LA-ICP-MS trace element study of the petrogenesis of garnet–cordierite–orthoamphibole gneisses from the Central Zone of the Limpopo Belt, South Africa. *Lithos* **88**, 150–172.

Burchfiel, B. C. & Royden, L. H. (1985). North–south extension within the convergent Himalayan region. *Geology* **13**, 679–682.

Burchfiel, B. C., Chen, Z. L., Hodges, K. V., Liu, Y. P., Royden, L. H., Deng, C. & Xie, J. (1992). The South Tibetan detachment system, Himalaya orogen: Extension contemporaneous with and parallel to shortening in a collisional mountain belt. *Geological Society of America, Special Papers* **269**, 1–41.

Carosi, R., Montomoli, C. & Visonà, D. (2007). A structural transect in the Lower Dolpo: Insights on the tectonic evolution of Western Nepal. *Journal of Asian Earth Sciences* **29**, 407–423.

Carosi, R., Montomoli, C., Rubatto, D. & Visonà, D. (2010). Late Oligocene high-temperature shear zones in the core of the Higher Himalayan Crystallines (Lower Dolpo, western Nepal). *Tectonics* **29**, TC4029.

Catlos, E. J., Gilley, L. D. & Harrison, T. M. (2002). Interpretation of monazite ages obtained via *in situ* analysis. *Chemical Geology* **188**, 193–215.

Cawood, P. A., Johnson, M. R. W. & Nemchin, A. A. (2007). Early Palaeozoic orogenesis along the Indian margin of Gondwana: Tectonic response to Gondwana assembly. *Earth and Planetary Science Letters* **255**, 70–84.

Cesare, B., Ferrero, S., Salvioli-Mariani, E., Pedron, D. & Cavallo, A. (2009). 'Nanogranite' and glassy inclusions: the anatectic melt in migmatites and granulites. *Geology* **37**, 627–630.

Chambers, J., Parrish, R., Argles, T., Harris, N. & Horstwood, M. (2011). A short-duration pulse of ductile normal shear on the outer South Tibetan detachment in Bhutan: Alternating channel flow and critical taper mechanics of the eastern Himalaya. *Tectonics* **30**, TC2005.

Cherniak, D. J. (2000). Pb diffusion in rutile. *Contributions to Mineralogy and Petrology* **139**, 198–207.

Cherniak, D. J., Watson, E. B., Grove, M. & Harrison, T. M. (2004). Pb diffusion in monazite: a combined RBS/SIMS study. *Geochimica et Cosmochimica Acta* **68**, 829–840.

Cherniak, D. J., Manchester, J. & Watson, E. B. (2007). Zr and Hf diffusion in rutile. *Earth and Planetary Science Letters* **261**, 267–279.

Corrie, S. L. & Kohn, M. J. (2011). Metamorphic history of the central Himalaya, Annapurna region, Nepal, and implications for tectonic models. *Geological Society of America Bulletin* **123**, 1863–1879.

Cottle, J. M., Jessup, M. J., Newell, D. L., Searle, M. P., Law, R. D. & Horstwood, M. S. A. (2007). Structural insights into the early stages of exhumation along an orogen-scale detachment: the South Tibetan detachment system, Dzakaa Chu section, eastern Himalaya. *Journal of Structural Geology* **29**, 1781–1797.

Cottle, J. M., Searle, M. P., Horstwood, M. S. A. & Waters, D. J. (2009). Timing of midcrustal metamorphism, melting, and deformation in the Mount Everest region of Southern Tibet revealed by U-(Th)-Pb geochronology. *Journal of Geology* **117**, 643–664.

DeCelles, P. G., Gehrels, G. E., Quade, J., LaReau, B. & Spurlin, M. (2000). Tectonic implications of U–Pb zircon ages of the Himalayan orogenic belt in Nepal. *Science* **288**, 497–499.

DeCelles, P. G., Robinson, D. M., Quade, J., Ojha, T. P., Garzione, C. N., Copeland, P. & Upreti, B. N. (2001). Stratigraphy, structure, and tectonic evolution of the Himalayan fold–thrust belt in western Nepal. *Tectonics* **20**, 487–509.

Eggins, S. M., Rudnick, R. L., McDonough, W. F. (1998). The composition of peridotites and their minerals: a laser ablation ICP-MS study. *Earth and Planetary Science Letters* **154**, 53–71.

England, P. C. & Thompson, A. B. (1984). Pressure–temperature–time paths of regional metamorphism I. Heat transfer during the evolution of regions of thickened continental crust. *Journal of Petrology* **25**, 894–928.

Ewing, T. A. (2011). Hf isotope analysis and U–Pb geochronology of rutile: Technique development and application to a lower crustal section (Ivrea–Verbano Zone, Italy). PhD thesis, Australian National University, Canberra, ACT, 385 pp.

Ewing, T. A., Hermann, J. & Rubatto, D. (2013). The robustness of the Zr-in-rutile and Ti-in-zircon thermometers during high-temperature metamorphism (Ivrea–Verbano Zone, northern Italy). *Contributions to Mineralogy and Petrology* **165**, 757–779.

Faccenda, M., Gerya, T. V. & Chakraborty, S. (2008). Styles of postsubduction collisional orogeny: influence of convergence velocity, crustal rheology and radiogenic heat production. *Lithos* **103(1–2)**, 257–287.

Ferrero, S., Bartoli, O., Cesare, B., Salvioli-Mariani, E., Acosta-Vigil, A., Cavallo, A., Groppo, C. & Battiston, S. (2012). Microstructures of melt inclusions in anatectic metasedimentary rocks. *Journal of Metamorphic Geology* **30**, 303–322.

Fletcher, I. R., McNaughton, N. J., Davis, W. J. & Rasmussen, B. (2010). Matrix effects and calibration limitations in ion probe U–Pb and Th–Pb dating of monazite. *Chemical Geology* **270**, 31–44.

Foster, G., Kinny, P., Vance, D., Prince, C. & Harris, N. (2000). The significance of monazite U–Th–Pb age data in metamorphic assemblages; a combined study of monazite and garnet chronometry. *Earth and Planetary Science Letters* **181**, 327–340.

Foster, G., Gibson, H. D., Parrish, R., Horstwood, M., Fraser, J. & Tindle, A. (2002). Textural, chemical and isotopic insights into the nature and behaviour of metamorphic monazite. *Chemical Geology* **191**, 183–207.

Foster, G., Parrish, R. R., Horstwood, M. S. A., Chenery, S., Pyle, J. & Gibson, H. D. (2004). The generation of prograde *P–T–t* points and paths; a textural, compositional, and chronological study of metamorphic monazite. *Earth and Planetary Science Letters* **228**, 125–142.

Fraser, G., Worley, B. & Sandiford, M. (2000). High-precision geothermobarometry across the High Himalayan metamorphic sequence, Langtang Valley, Nepal. *Journal of Metamorphic Geology* **18**, 665–681.

From, R. & Larson, K. (2014). Tectonostratigraphy, deformation, and metamorphism of the Himalayan mid-crust exposed in the Likhu Khola region, east–central Nepal. *Geosphere* **10**, 292–307.

From, R., Larson, K. & Cottle, J. M. (2014). Metamorphism and geochronology of the exhumed Himalayan midcrust, Likhu Khola region, east–central Nepal: Recognition of a tectonometamorphic discontinuity. *Lithosphere* **6**, 361–376.

Gleadow, A. J. W. & Duddy, I. R. (1981). A natural long-term track annealing experiment for apatite. *Nuclear Tracks* **5**, 169–174.

Godin, L., Grujic, D., Law, R. D. & Searle, M. P. (2006). Channel flow, ductile extrusion and exhumation in continental collision zones: an introduction. In: Law, R. D., Searle, M. P. & Godin, L. (eds) *Channel Flow, Ductile Extrusion and Exhumation in Continental Collision Zones. Geological Society, London, Special Publications* **268**, 1–23.

Goscombe, B., Gray, D. & Hand, M. (2006). Crustal architecture of the Himalayan metamorphic front in eastern Nepal. *Gondwana Research* **10**, 232–255.

Gregory, C. J., Rubatto, D., Allen, C. M., Williams, I. S., Hermann, J. & Ireland, T. (2007). Allanite micro-geochronology: A LA-ICP-MS and SHRIMP U–Th–Pb study. *Chemical Geology* **245**, 162–182.

Groppo, C., Rolfo, F. & Lombardo, B. (2009). *P–T* evolution across the Main Central Thrust Zone (Eastern Nepal): hidden discontinuities revealed by petrology. *Journal of Petrology* **50**, 1149–1180.

Groppo, C., Rolfo, F. & Indares, A. (2012). Partial melting in the Higher Himalayan Crystallines of Eastern Nepal: the effect of decompression and implications for the 'Channel Flow' model. *Journal of Petrology* **53**, 1057–1088.

Groppo, C., Rolfo, F. & Mosca, P. (2013). The cordierite-bearing anatectic rocks of the Higher Himalayan Crystallines (eastern Nepal): low-pressure anatexis, meltproductivity, melt loss and the preservation of cordierite. *Journal of Metamorphic Geology* **31**, 187–204.

Groppo, C., Rubatto, D., Rolfo, F. & Lombardo, B. (2010). Early Oligocene partial melting in the Main Central Thrust Zone (Arun valley, eastern Nepal Himalaya). *Lithos* **118(3–4)**, 287–301.

Grujic, D., Casey, M., Davidson, C., Hollister, L. S., Kuendig, R., Pavlis, T. L. & Schmid, S. M. (1996). Ductile extrusion of the Higher Himalayan Crystalline in Bhutan: Evidence from quartz microfabrics. *Tectonophysics* **260**, 21–43.

Grujic, D., Warren, C. J. & Wooden, J. L. (2011). Rapid synconvergent exhumation of Miocene-aged lower orogenic crust in the eastern Himalaya. *Lithosphere* **3**, 346–366.

Hames, W. E. & Bowring, S. A. (1994). An empirical evaluation of the argon diffusion geometry in muscovite. *Earth and Planetary Science Letters* **124**, 161–169.

Harris, N. B. W., Caddick, M., Kosler, J., Goswami, S., Vance, D. & Tindle, A. G. (2004). The pressure -temperature -time path of migmatites from the Sikkim Himalaya. *Journal of Metamorphic Geology* **22**, 249–264.

Harrison, T. M., McKeegan, K. D. & LeFort, P. (1995). Detection of inherited monazite in the Manaslu leucogranite by $^{208}Pb/^{232}Th$ ion microprobe dating: Crystallization age and tectonic implications. *Earth and Planetary Science Letters* **133**, 271–282.

Harrison, T. M., Ryerson, F. J., Le Fort, P., Yin, A., Lovera, O. M. & Catlos, E. J. (1997). A Late Miocene–Pliocene origin for the Central Himalayan inverted metamorphism. *Earth and Planetary Science Letters* **146**, E1–E7.

Henry, P., Le Pichon, X. & Goffé, B. (1997). Kinematic, thermal and petrological model of the Himalayas: constraints related to metamorphism within the underthrust Indian crust and topographic elevation. *Tectonophysics* **273**, 31–56.

Hermann, J. & Rubatto, D. (2003). Relating zircon and monazite domains to garnet growth zones: age and duration of granulite facies metamorphism in the Val Malenco lower crust. *Journal of Metamorphic Geology* **21**, 833–852.

Hollister, L. S. & Grujic, D. (2006). Pulsed channel flow in Bhutan. In: Law, R. D., Searle, M. P. & Godin, L. (eds) *Channel Flow, Ductile Extrusion and Exhumation in Continental Collision Zones. Geological Society, London, Special Publications* **268**, 415–423.

Icenhower, J. & London, D. (1995). An experimental study of element partitioning among biotite, muscovite, and coexisting peraluminous silicic melt at 200 MPa (H_2O). *American Mineralogist* **80**, 1229–1251.

Imayama, T. & Suzuki, K. (2013). Carboniferous inherited grain and age zoning of monazite and xenotime from leucogranites in far-eastern Nepal: Constraints from electron probe microanalysis. *American Mineralogist* **98**, 1393–1406.

Imayama, T., Takeshita, T. & Arita, K. (2010). Metamorphic *P–T* profile and *P–T* path discontinuity across the far-eastern Nepal Himalaya: investigation of channel flow models. *Journal of Metamorphic Geology* **28**, 527–549.

Imayama, T., Takeshita, T., Yi, K., Cho, D.-L., Kitajima, K., Tsutsumi, Y., Kayama, M., Nishido, H., Okumura, T., Yagi, K., Itaya, T. & Sano, Y. (2012). Two-stage partial melting and contrasting cooling history within the Higher Himalayan Crystalline Sequence in the far-eastern Nepal Himalaya. *Lithos* **134–135**, 1–22.

Ishida, T. (1969). Petrography and structure of the area between the Dudh Kosi and Tamba Kosi, East Nepal. *Journal of the Geological Society of Japan* **75**(**3**), 115–125.

Ishida, T. & Ohta, Y. (1973). Ramechhap–Okhaldhunga region. In: Hashimoto, S., Ohta, Y., Akiba, C. & Daigaku, H. (eds) *Geology of the Nepal Himalayas*. Saikon Publishing Company, pp. 39–68.

Jamieson, R. A. & Beaumont, C. (2013). On the origin of orogens. *Geological Society of America Bulletin* **125**, 1671–1702.

Jamieson, R. A., Beaumont, C., Medvedev, S. & Nguyen, M. H. (2004). Crustal channel flows: 2. Numerical models with implications for metamorphism in the Himalayan–Tibetan orogen. *Journal of Geophysical Research B: Solid Earth* **109**, B06407.

Jamieson, R. A., Beaumont, C., Nguyen, M. H. & Grujic, D. (2006). Provenance of the Greater Himalayan sequence and associated rocks: predictions of channel flow models. In: Channel Flow, Ductile Extrusion and Exhumation in Continental Collision Zones. Law, R. D., Searle, M. P. & Godin, L. (eds) *Geological Society of London Special Publication* **268**, 165–182.

Janots, E., Brunet, F., Goffé, B., Poinssot, C., Burchard, M. & Cemič, L. (2007). Thermochemistry of monazite-(La) and dissakisite-(La): implications for monazite and allanite stability in metapelites. *Contributions to Mineralogy and Petrology* **154**, 1–14.

Jiao, S., Guo, J., Mao, Q. & Zhao, R. (2011). Application of Zr-in-rutile thermometry: a case study from ultrahigh-temperature granulites of the Khondalite belt, North China Craton. *Contributions to Mineralogy and Petrology* **162**, 379–393.

Kellett, A. D., Grujic, D., Warren, C., Cottle, J., Jamieson, R. & Tenzin, T. (2010). Metamorphic history of a syn-convergent orogen-parallel detachment: The South Tibetan detachment system, Bhutan Himalaya. *Journal of Metamorphic Geology* **28**, 785–808.

Kohn, M. J. (2008). *P–T–t* data from central Nepal support critical taper and repudiate large-scale channel flow of the Greater Himalayan Sequence. *Geological Society of America Bulletin* **120**, 259–273.

Kohn, M. J. & Corrie, S. L. (2011). Preserved Zr-temperatures and U–Pb ages in high-grade metamorphic titanite: Evidence for a static hot channel in the Himalayan orogen. *Earth and Planetary Science Letters* **311**, 136–143.

Kohn, M. J. & Malloy, M. A. (2004). Formation of monazite via prograde metamorphic reactions among common silicates: implications for age determinations. *Geochimica et Cosmochimica Acta* **68**, 101–113.

Kohn, M. J., Wieland, M. S., Parkinson, C. D. & Upreti, B. N. (2004). Miocene faulting at plate tectonic velocity in the Himalaya of central Nepal. *Earth and Planetary Science Letters* **228**, 299–310.

Kooijman, E., Mezger, K. & Berndt, J. (2010). Constraints on the U–Pb systematics of metamorphic rutile from *in situ* LA-ICP-MS analysis. *Earth and Planetary Science Letters* **293**, 321–330.

Kooijman, E., Smit, M. A., Mezger, K. & Berndt, J. (2012). Trace element systematics in granulite facies rutile: implications for Zr geothermometry and provenance studies. *Journal of Metamorphic Geology* **30**, 397–412.

Lanzirotti, A. (1995). Yttrium zoning in metamorphic garnets. *Geochimica et Cosmochimica Acta* **59**, 4105–4110.

Larson, K., Godin, L. & Price, R. A. (2010). Relationships between displacement and distortion in orogens: Linking the Himalayan foreland and hinterland in central Nepal. *Geological Society of America Bulletin* **122**, 1116–1134.

Larson, K., Cottle, J. M. & Godin, L. (2011). Petrochronologic record of metamorphism and melting in the upper Greater Himalayan sequence, Manaslu–Himal Chuli Himalaya, west–central Nepal. *Lithosphere* **3**(**6**), 379–392.

Larson, K. P. (2012). The geology of the Tama Kosi and Rolwaling valley region, East–Central Nepal. *Geosphere* **8**, 507–517.

Larson, K. P. & Cottle, J. M. (2014). Mid-crustal discontinuities and the assembly of the Himalayan mid-crust. *Tectonics* **33**(**5**), 718–740.

Larson, K. P., Gervais, F. & Kellett, D. A. (2013). A *P–T–t–D* discontinuity in east–central Nepal: Implications for the evolution of the Himalayan mid-crust. *Lithos* **179**, 275–292.

Lederer, G. W., Cottle, J. M., Jessup, M. J., Langille, J. M. & Ahmad, T. (2013). Timescales of partial melting in the Himalayan middle crust: insight from the Leo Pargil dome, northwest India. *Contributions to Mineralogy and Petrology* **166**, 1415–1441.

Leech, M. L., Singh, S., Jain, A. K., Klemperer, S. L. & Manickavasagam, R. M. (2005). The onset of India–Asia continental collision: Early, steep subduction required by the timing of UHP metamorphism in the western Himalaya. *Earth and Planetary Science Letters* **234**, 83–97.

Le Fort, P. (1975). Himalayas: the collided range. Present knowledge of the continental arc. *American Journal of Science* **275a**, 1–44.

Liu, X., Liu, X., Leloup, P. H., Maheo, G., Paquette, J. L., Zhang, X. & Zhou, X. (2012). Ductile deformation within Upper Himalaya Crystalline Sequence and geological implications, in Nyalam area, Southern Tibet. *Chinese Science Bulletin* **57**, 3469–3481.

Ludwig, K. R. (2008). *Isoplot/Ex version 3.7. A geochronological toolkit for Microsoft Excel. Berkeley Geochronological Centre, Special Publication*. [available at: http://www.bgc.org/isoplot_etc/isoplot.html].

Martin, A. J., Gehrels, G. E. & DeCelles, P. G. (2007). The tectonic significance of (U,Th)/Pb ages of monazite inclusions

in garnet from the Himalaya of central Nepal. *Chemical Geology* **244**, 1–24.

Martin, A. J., Ganguly, J. & DeCelles, P. G. (2010). Metamorphism of Greater and Lesser Himalayan rocks exposed in the Modi Khola valley, central Nepal. *Contributions to Mineralogy and Petrology* **159**, 203–223.

McDonough, W. F. & Sun, S. (1995). The composition of the Earth. *Chemical Geology* **120**, 223–253.

Montomoli, C., Iaccarino, S., Carosi, R., Langone, A. & Visonà, D. (2013). Tectonometamorphic discontinuities within the Greater Himalayan Sequence in Western Nepal (Central Himalaya): Insights on the exhumation of crystalline rocks. *Tectonophysics* **608**, 1349–1370.

Mottram, C. M., Warren, C. J., Regis, D., Roberts, N. M. W., Harris, N. B. W., Argles, T. W. & Parrish, R. R. (2014). Developing an inverted Barrovian sequence; insights from monazite petrochronology. *Earth and Planetary Science Letters* **403**, 418–431.

Myrow, P. M., Hughes, N. C., Searle, M. P., Fanning, C. M., Peng, S. C. & Parcha, S. K. (2009). Stratigraphic correlation of Cambrian–Ordovician deposits along the Himalaya: Implications for the age and nature of rocks in the Mount Everest region. *Geological Society of America Bulletin* **121**, 323–332.

Nelson, K. D., Zhao, W., Brown, L. D., et al. (1996). Partially molten middle crust beneath southern Tibet; synthesis of Project INDEPTH results. *Science* **274**, 1684–1688.

Parrish, R. R. (1990). U–Pb dating of monazite and its application to geological problems. *Canadian Journal of Earth Sciences* **27**, 1431–1450.

Paton, C., Woodhead, J. D., Hellstrom, J. C., Hergt, J. M., Greig, A. & Maas, R. (2010). Improved laser ablation U–Pb zircon geochronology through robust downhole fractionation correction. *Geochemistry, Geophysics, Geosystems* **11**, Q0AA06.

Pearson, O. N. & DeCelles, P. G. (2005). Structural geology and regional tectonic significance of the Ramgarh Thrust, Himalayan fold–thrust belt of Nepal. *Tectonics* **24**, doi:10.1029/2003TC001617.

Pyle, J. M., Spear, F. S., Rudnick, R. L. & McDonough, W. F. (2001). Monazite–xenotime–garnet equilibrium in metapelites and a new monazite–garnet thermometer. *Journal of Petrology* **42**, 2083–2107.

Reddy, S. M., Searle, M. P. & Massey, J. A. (1993). Structural evolution of the High Himalayan Gneiss sequence, Langtang valley, Nepal. In: Treloar, P. J. & Searle, M. P. (eds) *Himalayan Tectonics. Geological Society, London, Special Publications* **74**, 375–389.

Robinson, D. M., DeCelles, P. G. & Copeland, P. (2006). Tectonic evolution of the Himalayan thrust belt in western Nepal: Implications for channel flow models. *Geological Society of America Bulletin* **118**, 865–885.

Rowley, D. B. (1996). Age of initiation of collision between India and Asia: A review of stratigraphic data. *Earth and Planetary Science Letters* **145**, 1–13.

Royden, L. H. (1993). Evolution of retreating subduction boundaries formed during continental collision. *Tectonics* **12**, 629–638.

Rubatto, D., Williams, I. S. & Buick, I. S. (2001). Zircon and monazite response to prograde metamorphism in the Reynolds Range, central Australia. *Contributions to Mineralogy and Petrology* **140**, 458–468.

Rubatto, D., Hermann, J. & Buick, I. S. (2006). Temperature and bulk composition control on the growth of monazite and zircon during low-pressure anatexis (Mount Stafford, central Australia). *Journal of Petrology* **47**, 1973–1996.

Rubatto, D., Chakraborty, S. & Dasgupta, S. (2013). Timescales of crustal melting in the Higher Himalayan Crystallines (Sikkim, Eastern Himalaya) inferred from trace element-constrained monazite and zircon chronology. *Contributions to Mineralogy and Petrology* **165**, 349–372.

Sawyer, E. W. & Brown, M. (2008). Working with Migmatites. *Mineralogical Association of Canada, Short Course Series* **38**, 12–13.

Schärer, U. (1984). The effect of initial ^{230}Th disequilibrium on young U–Pb ages: the Makalu case, Himalaya. *Earth and Planetary Science Letters* **67**, 191–204.

Schelling, D. (1992). The tectonostratigraphy and structure of the eastern Nepal Himalaya. *Tectonics* **11**, 925–943.

Searle, M. P. & Szulc, A. G. (2005). Channel flow and ductile extrusion of the high Himalayan slab—the Kangchenjunga–Darjeeling profile, Sikkim Himalaya. *Journal of Asian Earth Sciences* **25**, 173–185.

Searle, M. P., Parrish, R. R., Hodges, K. V., Hurford, A., Ayres, M. W. & Whitehouse, M. J. (1997). Shisha Pangma leucogranite, South Tibet: field relations, age, origin and emplacement. *Journal of Geology* **105**, 295–315.

Searle, M. P., Simpson, R. L., Law, R. D., Parrish, R. R. & Waters, D. J. (2003). The structural geometry, metamorphic and magmatic evolution of the Everest massif, High Himalaya of Nepal–South Tibet. *Journal of Geological Society, London* **160**, 345–366.

Searle, M. P., Law, R. D., Godin, L., Larson, K. P., Streule, M. J., Cottle, J. M. & Jessup, M. J. (2008). Defining the Himalayan Main Central Thrust in Nepal. *Journal of the Geological Society, London* **165**, 523–534.

Sorcar, N., Hoppe, U., Dasgupta, S. & Chakraborty, S. (2014). High-temperature cooling histories of migmatites from the High Himalayan Crystallines in Sikkim, India: rapid cooling unrelated to exhumation?. *Contributions to Mineralogy and Petrology* **167**, 1–34.

Spear, F. S. & Pyle, J. M. (2010). Theoretical modeling of monazite growth in a low-Ca metapelite. *Chemical Geology* **273**, 111–119.

Stacey, J. S. & Kramers, J. D. (1975). Approximation of terrestrial lead evolution by a two-stage model. *Earth and Planetary Science Letters* **26**, 207–221.

Stearns, M. A., Hacker, B. R., Ratschbacher, L., Lee, J., Cottle, J. M. & Kylander-Clark, A. (2013). Synchronous Oligocene–Miocene metamorphism of the Pamir and the north Himalaya driven by plate-scale dynamics. *Geology* **41**, 1071–1074.

Steiger, R. & Jäger, E. (1977). Subcommission on geochronology: convention on the use of decay constants in geo- and cosmo-chronology. *Earth and Planetary Science Letters* **36**, 359–362.

Tagami, T., Galbraith, R. F., Yamada, R. & Laslett, G. M. (1998). Revised annealing kinetics of fission tracks in zircon and geological implications. In: Van den Haute, P. & de Corte, F. (eds) *Advances in Fission-Track Geochronology, 10*. Kluwer Academic, pp. 99–112.

Tomkins, H. S., Powell, R. & Ellis, D. J. (2007). The pressure dependence of the zirconium-in-rutile thermometer. *Journal of Metamorphic Geology* **25**, 703–713.

Vry, J. K. & Baker, J. A. (2006). LA-MC-ICPMS Pb–Pb dating of rutile from slowly cooled granulites: Confirmation of the high closure temperature for Pb diffusion in rutile. *Geochimica et Cosmochimica Acta* **70**, 1807–1820.

Wang, A., Garver, J. I., Wang, G., Smith, J. A. & Zhang, K. (2010). Episodic exhumation of the Greater Himalayan Sequence since the Miocene constrained by fission track thermochronology in Nyalam, central Himalaya. *Tectonophysics* **495**, 315–323.

Wang, J. M., Zhang, J. J. & Wang, X. X. (2013). Structural kinematics, metamorphic *P–T* profiles and zircon geochronology across the Greater Himalayan Crystalline Complex in south–central Tibet: implication for a revised channel flow. *Journal of Metamorphic Geology* **31**, 607–628.

Wang, J. M., Zhang, J. J., Wei, C. J., Rai, S. M., Wang, M. & Qian, J. H. (2015). Characterising the metamorphic discontinuity across the Main Central Thrust Zone of eastern–central Nepal. *Journal of Asian Earth Sciences* **101**, 83–100.

Wang, Y., Li, Q. & Qu, G. (2006). $^{40}Ar/^{39}Ar$ thermochronological constraints on the cooling and exhumation history of the South Tibetan Detachment System, Nyalam area, southern Tibet. In: Law, R. D., Searle, M. P. & Godin, L. (eds) *Channel Flow, Ductile Extrusion and Exhumation in Continental Collision Zones. Geological Society, London, Special Publications* **268**, 327–354.

Warren, C. J., Grujic, D., Kellett, D. A., Cottle, J., Jamieson, R. A. & Ghalley, K. S. (2011). Probing the depths of the India–Asia collision: U–Th–Pb monazite chronology of granulites from NW Bhutan. *Tectonics* **30**, TC2004.

Watson, E. B., Wark, D. A. & Thomas, J. B. (2006). Crystallization thermometers for zircon and rutile. *Contributions to Mineralogy and Petrology* **151**, 413–433.

Webb, A. A. G., Schmitt, A. K., He, D. & Weigand, E. L. (2011). Structural and geochronological evidence for the leading edge of the Greater Himalayan Crystalline complex in the central Nepal Himalaya. *Earth and Planetary Science Letters* **304**, 483–495.

Whitney, D. L. & Evans, B. W. (2010). Abbreviations for names of rock-forming minerals. *American mineralogist* **95**, 185–187.

Williams, I. S. (1998). U–Th–Pb geochronology by ion microprobe. In: McKibben, M. A., Shanks, W. C. III , & Ridley, W. I. (eds) *Application of Microanalytical Techniques to Understanding Mineralizing Processes. Society of Economic Geologists, Reviews in Economic Geology* **7**, 1–35.

Williams, M. L., Jercinovic, M. J. & Hetherington, C. J. (2007). Microprobe monazite geochronology: understanding geologic processes by integrating composition and chronology. *Annual Review of Earth and Planetary Sciences* **35**, 137–175.

Wing, B. A., Ferry, J. M. & Harrison, T. M. (2003). Prograde destruction and formation of monazite and allanite during contact and regional metamorphism of pelites: petrology and geochronology. *Contributions to Mineralogy and Petrology* **145**, 228–250.

Xu, Z. Q., Wang, Q., Pêcher, A., Liang, F. H., Qi, X. X., Cai, Z. H., Li, H. Q., Zeng, L. S. & Cao, H. (2013). Orogen-parallel ductile extension and extrusion of the Greater Himalaya in the late Oligocene and Miocene. *Tectonics* **32**, 191–215.

Yin, A. (2006). Cenozoic tectonic evolution of the Himalayan orogen as constrained by along-strike variation of structural geometry, exhumation history, and foreland sedimentation. *Earth-Science Reviews* **76**, 1–131.

Zack, T., Stockli, D., Luvizotto, G., Barth, M., Belousova, E., Wolfe, M. & Hinton, R. (2011). *In situ* U–Pb rutile dating by LA-ICP-MS: ^{208}Pb correction and prospects for geological applications. *Contributions to Mineralogy and Petrology* **162**, 515–530.

Zhang, X. G., Liu, X. H., Liu, X. B. & Zhou, X. J. (2012). Metamorphism of mafic enclaves in central greater Himalaya sequence and its tectonic implication. *Chinese Journal of Geology* **2**, 278–289 (in Chinese with English abstract).

Zhang, Z. M., Xiang, H., Dong, X., Ding, H. X. & He, Z. Y. (2015). Long-lived high-temperature granulite-facies metamorphism in the Eastern Himalayan orogen, south Tibet. *Lithos* **212–215**, 1–15.

Zheng, Y., Zhang, J., Wang, J., Zhang, B., Wang, X. & Wang, M. (2014). Rapid denudation of the Himalayan orogen in the Nyalam area, southern Tibet, since the Pliocene and implications for tectonics–climate coupling. *Chinese Science Bulletin* **59**, 874–885.